Journal of
Manufacturing and Materials Processing

MDPI

Review

A Review of Modeling, Simulation, and Process Qualification of Additively Manufactured Metal Components via the Laser Powder Bed Fusion Method

Emmanuel De Leon [1,2,*], Alex Riensche [1,3], Benjamin D. Bevans [1,3], Christopher Billings [1,2], Zahed Siddique [1,2] and Yingtao Liu [1,2]

[1] Sooner Advanced Manufacturing Laboratory, The University of Oklahoma, Norman, OK 73019, USA; ariensche@ou.edu (A.R.); benjamin.bevans@ou.edu (B.D.B.); christopherbillings@ou.edu (C.B.); zsiddique@ou.edu (Z.S.); yingtao@ou.edu (Y.L.)
[2] School of Aerospace and Mechanical Engineering, The University of Oklahoma, Norman, OK 73019, USA
[3] School of Industrial and Systems Engineering, The University of Oklahoma, Norman, OK 73019, USA
* Correspondence: emmanuel.deleon@ou.edu

Abstract: Metal additive manufacturing (AM) has grown in recent years to supplement or even replace traditional fabrication methods. Specifically, the laser powder bed fusion (LPBF) process has been used to manufacture components in support of sustainment issues, where obsolete components are hard to procure. While LPBF can be used to solve these issues, much work is still required to fully understand the metal AM technology to determine its usefulness as a reliable manufacturing process. Due to the complex physical mechanisms involved in the multiscale problem of LPBF, repeatability is often difficult to achieve and consequently makes meeting qualification requirements challenging. The purpose of this work is to provide a review of the physics of metal AM at the melt pool and part scales, thermomechanical simulation methods, as well as the available commercial software used for finite element analysis and computational fluid dynamics modeling. In addition, metal AM process qualification frameworks are briefly discussed in the context of the computational basis established in this work.

Keywords: metal additive manufacturing; multiscale physics; process simulation; multiscale simulation; process qualification; laser powder bed fusion

Academic Editor: Fulvio Lavecchia

Received: 2 December 2024
Revised: 4 January 2025
Accepted: 11 January 2025
Published: 13 January 2025

Citation: De Leon, E.; Riensche, A.; Bevans, B.D.; Billings, C.; Siddique, Z.; Liu, Y. A Review of Modeling, Simulation, and Process Qualification of Additively Manufactured Metal Components via the Laser Powder Bed Fusion Method. *J. Manuf. Mater. Process.* **2025**, *9*, 22. https://doi.org/10.3390/jmmp9010022

1. Introduction

Metal additive manufacturing (AM) has grown in recent years to supplement traditional manufacturing methods in the spaces of design, parts production, and even component repair. Whereas the AM technology was largely used for rapid prototyping, it has now gained in popularity to become a part of mainstream manufacturing processes [1,2]. In several cases, metal AM has been used to replace traditional manufacturing methods due to its ability to manufacture low volume complex components more cheaply [3]. As parts age in older systems and become obsolete, they consequently become more difficult to procure. Therefore, it becomes challenging to source these parts at a reasonable price due to a high initial investment by manufacturing facilities to set up tooling, material, and manpower [4]. Metal AM avoids this as the only setup required is the fabrication machine itself, which makes producing low volume complex components more favorable [5].

The laser powder bed fusion (LPBF) process has emerged as a popular form of metal AM; it is depicted in Figure 1. The metal powder is raked across the build plate and is

melted with a high-power laser [6] including, but not limited to, YAG [7,8] and CO_2 [9,10] laser sources. The build piston is then lowered, and a new layer of powder is deposited. This process continues until the part is fully built. The chamber is typically filled with an inert gas environment like argon or nitrogen to reduce the risk of oxidation of the part during the micro-welding process [11].

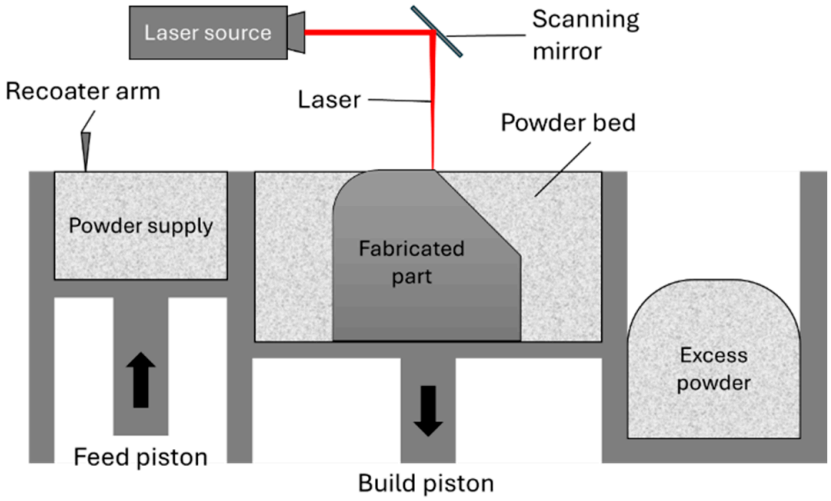

Figure 1. Typical internal schematic of an LPBF machine.

In the LPBF process, the key parameters involved in the manufacturing process can be categorized as follows [5]:

- Processing: laser power, laser spot size, scan velocity, scan strategy, hatching space.
- Material: alloy powder, powder size distribution, packing density, layer thickness, build plate temperature.
- Chamber environment: build volume, inert gas, gas flow speed, chamber temperature.

While this list is not comprehensive, as there are hundreds of process parameters involved both controllable and uncontrollable, a combination of them must be regulated and checked to ensure that the part can be printed with the desired material properties. In tandem, the process itself must be repeatable [12].

Despite advances in the usage of metal AM as innovative solutions in support of the production of both new and old components, the issue of process repeatability remains a large issue in accepting it as a reliable manufacturing method [4,13]. In LPBF, part related defects and errors can present themselves in the form of porosity, cracks, and delamination due to exceeding tensile stresses at the layer interfaces exceeding the yield stress of the alloy [14], incorrect scanning, part warpage, and distortion from developed residual stresses [15], and the recoater crashes [16,17]. In the melt pool scale, defects, such as gas porosities, keyholing, and lack of fusion, can manifest during the manufacturing process [18]. An understanding of these defects and how to minimize their effects through post-processing treatments can help improve the mechanical behavior of LPBF components [19]. Samples of these defects are shown in Figure 2. Current efforts in process qualification rely on destructive testing of coupons to obtain and validate material properties [16]. This can be costly, as destructive testing generally demands large quantities of powder material and significant manpower to prepare, build, and test coupons. Furthermore, destructive testing typically has an extensive cost in regard to time depending on the number of samples and type of test [4,13].

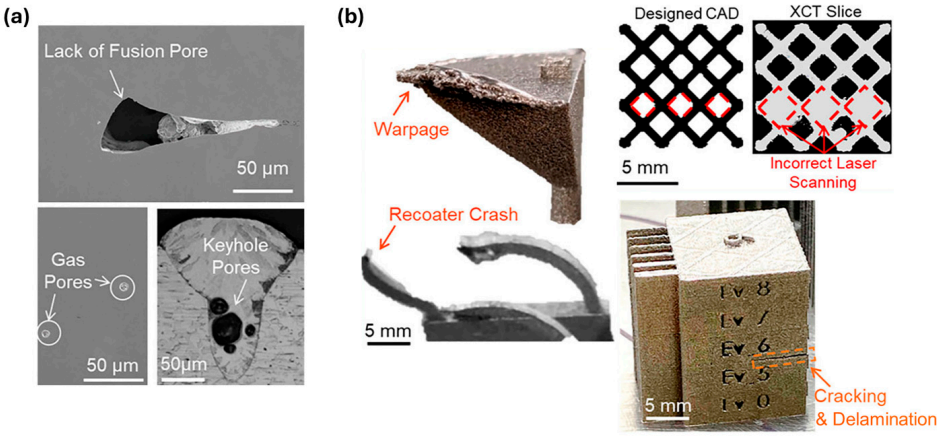

Figure 2. Sample of LPBF manufacturing process defects and errors in (**a**) the melt pool scale and (**b**) the part scale (adapted from Bevans et al. [17]).

Major developments have been made in using computer-aided design (CAD), computer-aided engineering (CAE), and computer-aided manufacturing (CAM) methods in alleviating the costly factors in producing physical test samples [20–22]. For example, thermomechanical modeling of LPBF aerospace components has been utilized as a qualification tool to quantify part quality and verification of the manufacturing process [23–25]. However, the reliability of the CAD/CAE/CAM methods to verify the LPBF process are dependent on the physical phenomena elucidated in simulation models [26]. Inherently, the LPBF process is a multiscale process that involves complex physics from the melt pool scale to the structural stress and distortions at the part scale [27]. Thus, the purpose of this work is to provide a review of the physical phenomena, analysis methods, modeling software, and process qualifications used in the LPBF process.

The rest of this paper is structured as follows: Section 2 discusses the multiscale phenomena in LPBF from the melt pool scale to the part scale. Part scale thermomechanical models and simulation methods of LPBF are examined in Section 3. In Section 4, commercial software available to model the LPBF process are compared, highlighting their capabilities and applications. Section 5 is focused on process qualification methods for LPBF components. Finally, an overall discussion and summary of the work presented are provided in Sections 6 and 7, respectively.

2. Physical Phenomena in the LPBF Process

As stated in the previous section, the LPBF process is a multiscale process, as many phenomena are involved to fully capture the physics involved in product manufacturing [27–29]. The length and time scales of the LPBF process are shown in Figure 3, where the phenomena scale can range from the melt pool scale to the entire part scale. With respect to time, the process scales from rapid melt pool formation all the way to the build time of the components. By understanding the physical phenomena in the LPBF process, strategies to select and optimize process parameters can be controlled to minimize defects, obtain proper material properties, and ensure the reliability of the manufacturing process. For example, optimization of process parameters for 316L steel can be used to obtain high densities and overcome limitations in the mechanical properties of traditional manufacturing by controlling the resulting microstructure [30]. The following section generalizes these scales into the physics at the melt pool scale and at the part scale.

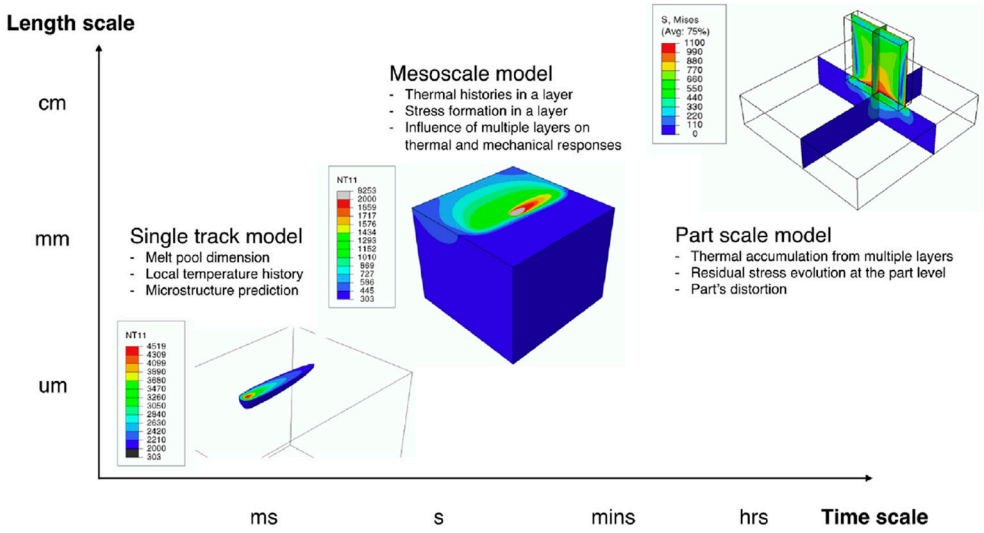

Figure 3. The multiscale relationships involved in the LPBF process [28].

2.1. Heat Source Models

To obtain proper mechanical responses, whether in the melt pool scale to elucidate grain structure evolution or in melt pool modes all the way to part scale thermal distortions and residual stresses, a proper thermal model must be used. Several models have been developed for heat sources [31–33] in analytical and energy sources for the heat equation. Rosenthal [34] was a pioneer in developing an analytical temperature solution for a moving heat source in welding applications for a semi-infinite solid; Goldak and Akhlaghi [35] summarized various models for welding heat sources including Gaussian, hemispherical, and ellipsoidal distributions; and Yang and Ayas [32] presented three treatments for modeling heat sources: point, surface, and volumetric heat sources for modeling the thermal scanning process of LPBF.

Table 1 lists the above power distribution equations along with an exact temperature solution as provided in its reference source. The utilization of a specific heat source model depends on the level of simplification required to improve computational efficiency.

Table 1. List of heat sources used in modeling temperature distributions in metal AM.

Heat Source Model	Equation	Reference
Rosenthal	$T = T_0 + \frac{\dot{q}}{2\pi kr}\exp\left(-\frac{v(r+\xi)}{2\alpha}\right)$	[34]
Gaussian Distribution	$q(r) = q(0)e^{-Cr^2}$	[35]
Hemispherical Distribution	$q(x,y,\xi) = \frac{6\sqrt{3}Q}{c^3\pi\sqrt{\pi}}\exp\left(-\frac{3x^2}{a^2}\right)\exp\left(-\frac{3y^2}{b^2}\right)\exp\left(-\frac{3\xi^2}{c^2}\right)$	[35]
Ellipsoidal Distribution	$q(x,y,z,t) = \frac{6\sqrt{3}Q}{abc\pi\sqrt{\pi}}\exp\left(-\frac{3x^2}{a^2}\right)\exp\left(-\frac{3y^2}{b^2}\right)\exp\left(-\frac{3[z+v(\tau-t)]^2}{c^2}\right)$	[35]
Point Heat Source	$Q = P\Delta t$ $T_p(x,t) = \frac{QA}{4\rho c_p(\pi\alpha(t-t_0))^{3/2}}\exp\left(-\frac{U^2}{4\alpha(t-t_0)}\right)$	[32]
Surface Heat Source	$Q_{ps} = \frac{2Q}{\pi r_l^2}\exp\left(-\frac{2r^2}{r_l^2}\right)$ $T_s = \omega\int_0^{r_l}\int_0^{2\pi}\frac{Q_{ps}}{4\rho c_p(\pi\alpha(t-t_0))^{3/2}}\exp\left(-\frac{U^2}{4\alpha(t-t_0)}\right)rd\theta\,dr$	[32]
Volumetric	$Q_{pv} = \frac{Q}{\delta}\exp\left(-\frac{U_3}{\delta}\right)$ $T_v = \zeta\int_0^{\delta}\int_0^{r_l}\int_0^{2\pi}\frac{Q_{pv}}{4\rho c_p(\pi\alpha(t-t_0))^{3/2}}\exp\left(-\frac{U^2}{4\alpha(t-t_0)}\right)rd\theta\,dr\,dx_3$	[32]

Naturally, the volumetric heat source closely represents the actual heating in the LPBF process, as both the surface and depth of the powder bed are penetrated by the laser source to melt material. However, using simplified models for the heat source can often lead to higher temperature predictions because the energy becomes more concentrated with each simplification level [32], as shown in Figure 4. When comparing laser models, Yang and Ayas [32] showed that point and surface models yield comparable results to each other and were also higher than the volumetric heat source. The resulting lower temperature is attributed to the laser's penetration depth, δ, in which a larger value correlates to a lower temperature. This is a direct result of the Beer–Lambert law, which states that the intensity of the radiation inside the material drops to 1/e of the initial density of the heat source, where e is Euler's number [36].

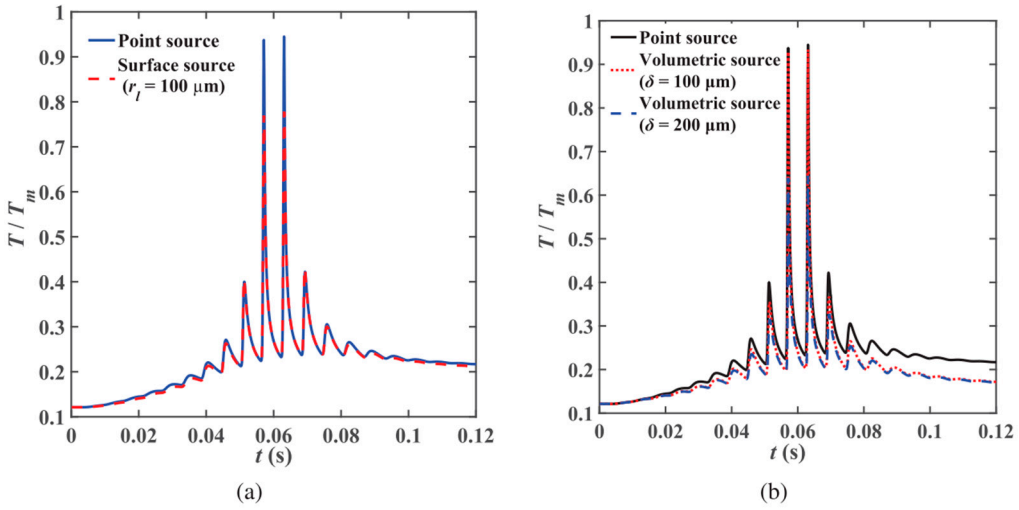

Figure 4. Comparison of normalized temperature histories by heat sources predicted by (**a**) point source and surface source models and (**b**) point source and volumetric source models with varying penetration depth. The temperatures T and T_m are predicted and melting temperatures, respectively [32].

2.2. Physical Phenomena at the Melt Pool Scale

The physical phenomena at the melt pool scale in the LPBF process is depicted in Figure 5. When the laser source heats the powder bed, solid powder particles are heated, changing phases to a liquid coalescing to a melt pool, then cooled completely to solidify as part of the solid structure of the part [36]. The process in which this occurs is in the time scale order of milliseconds due to high scan speeds ranging from about 100 to 1000 mm/s and rapid solidification rates in the order of 10^6 K/s [37]. The length scale is in the order of micrometers due to the size of metal powder particle sizes ranging from 10 to 100 μm as well as laser spot sizes of tens of micrometers [38,39]. This process is highly dependent on properties such as the laser exposure time, powder layer thickness, size of the laser beam itself, as well as the thermal properties of the material.

The fundamental phenomena involved in melt pool dynamics is dependent on the conservation equations of mass in Equation (1), momentum in Equation (2), and energy in Equation (3), respectively:

$$\frac{\partial \rho}{\partial t} + \nabla \cdot \rho \boldsymbol{v} = 0 \tag{1}$$

$$\rho \left[\frac{\partial \boldsymbol{v}}{\partial t} + (\boldsymbol{v} \cdot \nabla)\boldsymbol{v} \right] = -\nabla P + S_m \tag{2}$$

$$\rho \frac{\partial h}{\partial t} - \rho(\boldsymbol{v} \cdot \nabla)h = \nabla \cdot (k \nabla T) + S_E \tag{3}$$

where ρ is the material density, t is time, v is the velocity vector, P is pressure, S_m represents the momentum sources related to the fluid dynamics in the melt pool, h is enthalpy, k is the thermal conductivity of the material, T is temperature, and S_E represents the energy sources that contribute to the heat transfer in the melt pool and its surroundings. Cook and Murphy [40] provide an excellent summary of the momentum and energy sources used in the modeling and simulation of the melt pool dynamics. Namely, the momentum sources include terms such as the viscosity of fluid, acceleration due to gravity, buoyancy, surface tension, and recoil pressure. In addition, the energy sources include the addition of the heat source, evaporation, radiation, and convection off the surface of the melt pool [40].

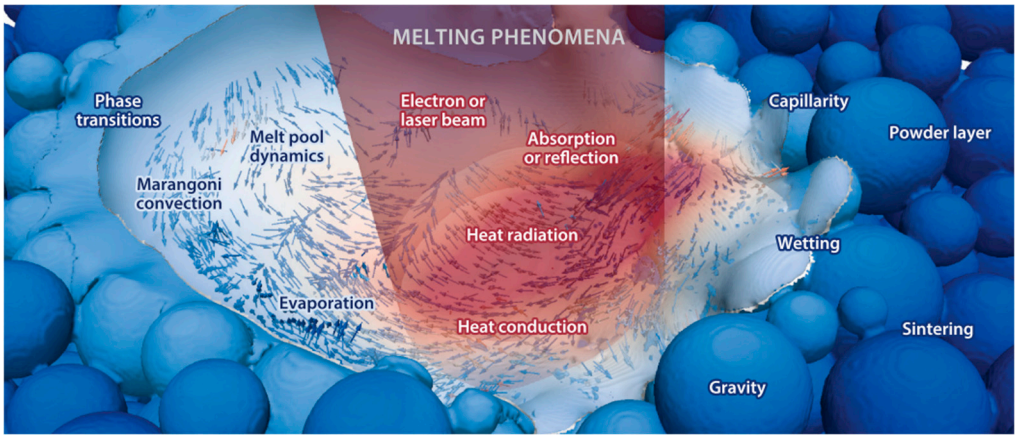

Figure 5. Physical phenomena at the melt pool scale [27].

The effects of process parameters on the evolution of the melt pool have been studied by various authors [9,37,41–45]. For example, Yang et al. [37] demonstrated that the melt pool shapes play a significant role in LPBF material properties for Ti-6Al-4V and identified the relationships in their formability, microstructural evolution, and mechanical properties. While the former study varied scanning speed, laser power, hatch spacing, and layer thickness, Qi et al. [43] also considered the defocusing distance of the laser, which was shown to impact the amount of laser energy absorbed by the powder bed inducing the two melt pool shapes, as shown in Figure 6. In addition, they also observed that varying the defocusing distance changes the morphology and distribution of cracks in builds.

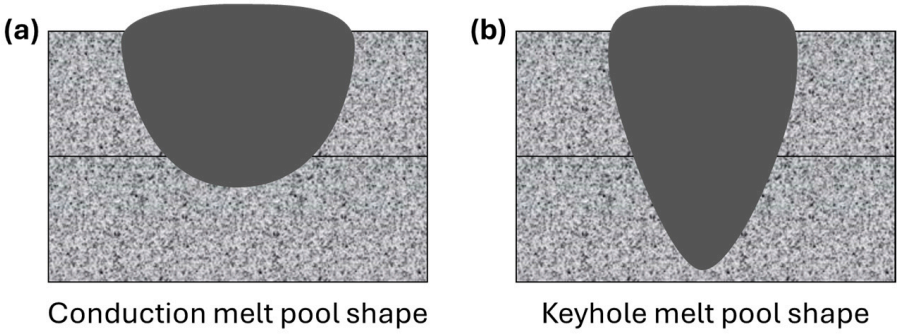

Figure 6. Two melt pool shapes in LPBF: (**a**) conduction melt pool and (**b**) keyhole melt pool.

A few observations can be made with the formation of the melt pool shapes with respect to melt pool dynamics [44,46]. In the conduction melt pool shape, as shown in Figure 6a, the laser energy is initially absorbed at the surface of the topmost powder particles, with the molten material accumulating due to surface tension. The liquid must have sufficient enthalpy to melt the underlying powder and solid material, so a strong bond is developed with the lower layers. By contrast, the keyhole melt pool shape—as

shown in Figure 6b—is characterized by intense metal evaporation [42], recoil pressure [47], and Marangoni flow [41], causing a deep vapor cavity that enables the laser to penetrate and absorb energy far deeper than in the conduction melt pool [48]. A more detailed visual explanation of melt pool dynamics was elaborated by Leung et al. [49] using in situ x-ray imaging. They were able to capture and quantify the mechanisms that influence the evolution of melt pool features and their morphology. To ensure control of the resulting quality of LPBF builds, process monitoring techniques, such as experimental designs [38] or machine learning [45], have the ability to produce consistent desired material properties during the manufacturing process.

With respect to the resulting part quality at the melt pool scale, Maamoun et al. [50,51] studied the effects of process parameters on Al alloy parts with respect to the volumetric energy density, E_d:

$$E_d = \frac{P_L}{v d_h t_l} \tag{4}$$

where P_L is the laser power, v is the scan speed, d_h is the hatch spacing, and t_l is the layer thickness. The authors of [50] determined that E_d affects relative density and porosity formation as higher E_d values induce gas pores, while lower E_d values contribute to keyhole pore formation due to lack of powder fusion. Also, with increasing E_d values, surface roughness is reduced. With respect to dimensional tolerance, the best surface flatness was obtained with higher d_h and v values. In addition, it was shown that grain structure can change with varying E_d [51].

2.3. Physical Phenomena at the Part Scale

When describing the physical phenomena of AM components in the part scale, or macroscale, analysis usually occurs in length scales from millimeters to meters, comprising fine part features (>1 mm) to completed parts tens of centimeters large [22]. The time scale for parts manufactured by the LPBF process can range from hours to several days, depending on the build size, as it is determined by the build time during the process. Referring again to Figure 1, it is useful to understand that the physical processes typically observed at the part scale include the layer-by-layer build, residual stresses developed, as well as the thermal deformation of builds.

When builds undergo the immense amount of heat in the LPBF process, heat is expected to accumulate within the previously melted layers [35,52]. The energy accumulation, however, is less than typical welding processes since the energy deposited in the LPBF process is highly localized and rapid, while thermal evolution is more gradual and less extreme at the part scale [53]. When measuring the thermal evolution in Ti-6Al-4V components, Hooper [54] determined that components experience temperature gradients from 5 to 20 K/μm and cooling rates of 1 to 40 K/μs. Depending on the geometry of the component, heat will dissipate in the part differently as bulk, solid materials have higher thermal conductivity when compared to powder particles [55]. More specifically, heat dissipates faster through conduction when surrounded by fully solidified material, whereas heat dissipation is slower when surrounded by unmelted powder, due to air gaps between the particles that hinder conduction. Solidified melt pools surrounded by powder particles can cause hotspots, exacerbating residual stresses and thermal deformation of the build [56]. Since the AM process is repetitive, in that previously printed layers are often cyclically heated and cooled, thermal deformation of the entire part is inevitable. This usually results in manufacturing errors related to build stoppages and defects, such as gas porosities, keyholing, and lack of fusion [18].

At the part scale, the fundamental relationships in which a printed part can be modeled is through the mechanical constitutive equations of stress and strain [57]:

$$\boldsymbol{\sigma} = \boldsymbol{D}\boldsymbol{\varepsilon}_{el} \tag{5}$$

$$\boldsymbol{\varepsilon} = \boldsymbol{\varepsilon}_{el} + \boldsymbol{\varepsilon}_{p} + \boldsymbol{\varepsilon}_{th} \tag{6}$$

where $\boldsymbol{\sigma}$ is the stress tensor, $\boldsymbol{D}$ is the stiffness tensor, and $\boldsymbol{\varepsilon}$ is the total strain tensor. As shown in Equation (6), the total strain tensor $\boldsymbol{\varepsilon}$ is composed of $\boldsymbol{\varepsilon}_{el}$, $\boldsymbol{\varepsilon}_{p}$, and $\boldsymbol{\varepsilon}_{th}$, which are the elastic, plastic, and thermal strains, respectively. The equations above are dependent on the temperature profile output from Equation (1) through (3) to model the mechanics of deformation and stresses developed in the part, quantified by Equation (5).

The evolution of stresses and strain can be studied at the melt pool scale and provide significant information on the final quality of the component at the part scale. However, there is a mismatch in connecting analysis at the melt pool scale to part scale [39,56]. While dimensional accuracy has been observed in terms of Equation (4) to show that contraction of the parts occurs with lower energy densities and oversized parts were observed with higher energy density values [50], it does not necessarily quantify the instantaneous evolution of stress and strain developed in as-printed components. The finer-scale physics related to melt pool formation, such as melt flow and rapid solidification, directly impact microstructural properties, but are unable to be fully captured at the part scale due to computational limitations. The reverse is also true, as will be discussed in the next section, part scale simulations use simplified thermal models to predict residual stresses and thermal distortion, not considering melt pool dynamics due to the complex computational power needed to incorporate its physics [58]. As there is a mismatch in the analysis between the melt pool and part scales, efforts have been made to alleviate and bridge this gap. A few of these methods are discussed in subsequent sections.

3. Part Scale Modeling and Simulation Methods

Computational modeling and comprehensive simulation tools are essential to elucidate the principal behaviors of any system. Since a major concern in the adoption of metal AM is the process repeatability and quality assurance, it is valuable to focus on developing the physical phenomena that occurs within a build. Issues such as lack of fusion porosity, melt pool mode effects, and microstructure heavily influence the final as-built part and its mechanical properties. Being informed of these effects influences the part's design and determines whether it can be manufactured via AM. A popular focus on achieving a comprehensive understanding of the metal AM technology is through the adoption of process–structure–property (p-s-p) perspective of modeling [5,22,59]. The p-s-p model is a concept that aims to link the LPBF process parameters to the material's microstructure and phase composition, and its resulting material strength properties [22].

A visual of the simulation driven/product design strategy that encompasses the p-s-p process is shown in Figure 7, where it illustrates how different modeling and simulation techniques are intertwined to predict and optimize the properties of metal AM components. The more process-driven aspects of the LPBF process, such as its parameters, tool path, build geometry, and thermal history, influence much of the thermal history and temperature distribution of the build. Then, the thermal history influences the structure-driven process where microstructure evolution [60,61] can be described from grain size, orientation, porosity, and residual stresses. Finally, microstructure data can be used to inform the property-driven process where constitutive modeling can be used to predict material properties, such as tensile strength and fatigue properties [62]. Utilizing the p-s-p approach in the LPBF process can be used to optimize the process by linking thermal conditions,

microstructure, and final material properties to ensure parts are built with high quality and precision.

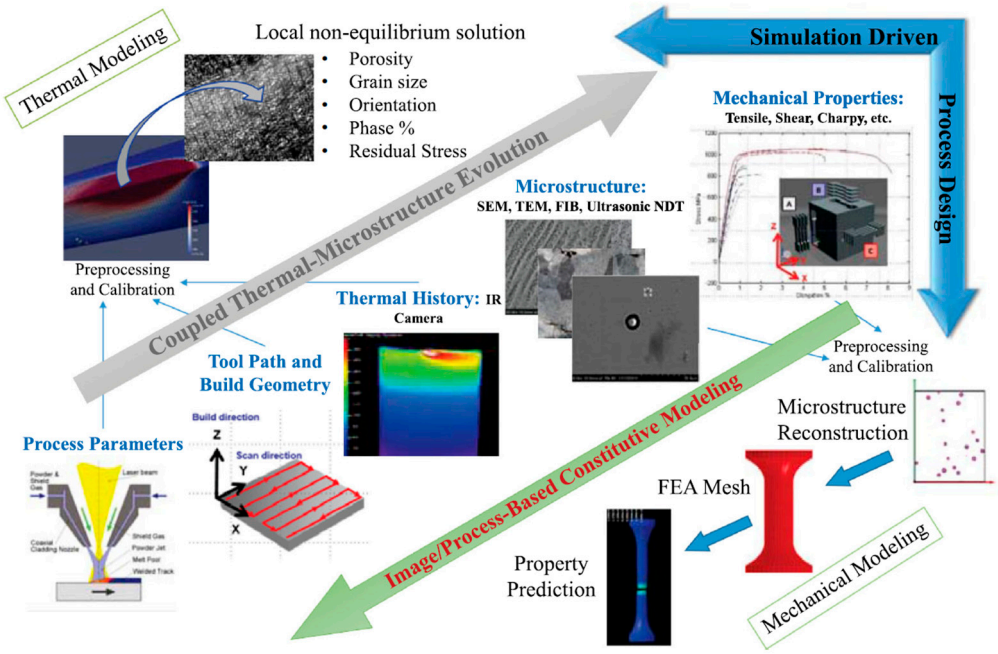

Figure 7. Paradigm of the process–structure–property modeling process of metal AM [5].

Incorporating a digital framework to design, analyze, and develop AM products enables users to develop a comprehensive understanding of the technology. However, the technology to perform various analyses in metal AM has yet to be fully integrated into such a computational modeling tool because building a multiscale predictive framework is challenging in its implementation and accuracy. Yan et al. [59] developed a p-s-p model for the selective electron beam melting (SEBM) of Ti-6Al-4V, generating an integrated framework that contains separate physics-based modules that feed into subsequent modules to ultimately predict yield strength and fatigue properties. The proposed framework effectively integrated various types of analyses related to the metal AM process, enabling the computational design of practical components. While development is still required in establishing a fully integrated modeling tool, the prospects of a multiscale analytical tool that encompasses the p-s-p model are achievable.

The subsequent sections discuss current methods in performing LPBF modeling and simulations to predict part scale residual stresses and thermal distortion from temperature field predictions. Multiple methods of obtaining temperature fields of metal AM build layers and components through coupled and decoupled thermomechanical approaches are discussed. It should be noted that all the methods examined below utilize finite element analysis (FEA) for predictive modeling and simulations.

3.1. Coupled Thermomechanical Models

Thermomechanical models utilize the fundamentals of welding mechanics when studying high thermal deformations in LPBF [63]. Leveraging from welding models as a basis, these models aim to predict stresses and resulting deformations in the manufacturing process. Alongside residual stresses, thermal deformations occur in the forms of thermal shrinkage, distortion, or warpage [35]. In layer AM processes, such as LPBF, previously printed layers that are solidified are subjected to repeated heating and remelting cycles [64,65], thereby making the formation of fully solidified objects in metal AM different than typical welding processes. It is critical that the process of modeling the

part scale stresses and distortions in the LPBF process captures essential physics related to temperature evolution within the manufactured component to accurately predict material properties and desired component performance through optimized parameters that meet requirements to qualify and accept the AM process and part.

In the following sections, three coupled thermomechanical methods for part scale analysis are discussed. It is coupled because the final structural analysis of the part being simulated is dependent on the resulting thermal analysis performed. The temperature history obtained from the thermal simulation is used as the input to the structural simulation to predict stresses and deformations.

3.1.1. Semi-Analytical Methods

The semi-analytical modeling approach aims to address the LPBF thermal process simulations utilizing the superposition principle for complete part build analysis [31,66]. It combines both analytical and numerical boundary value problems (BVPs) to predict thermal field evolution by representing the moving laser source with a finite number of point heat sources. In this method, the heat equation

$$\rho c_p \frac{\partial T}{\partial t} = \nabla \cdot (k \nabla T) + Q_v \tag{7}$$

is solved where c_p is constant-pressure specific heat of the material and Q_v is the rate of volumetric heat generation. While c_p can be a function to temperature [67], it is assumed to be a constant to simplify calculations. In addition, Q_v is a function of space and time and represents the heat generated by the laser heat source during the local scans in the LPBF process [33]. It should be noted that the temperature field solution does not capture the phenomena observed in the melt pool scale due to assumptions of temperature independent properties. The entire domain of the printed component and surrounding environment of the powder layer and baseplate are geometrically decomposed to its boundaries, as shown in Figure 8a and 8b, respectively. The basic overview of the temperature of the body, as shown in Figure 8c, is mathematically composed as follows:

$$T = \widetilde{T} + \hat{T} + \check{T} \tag{8}$$

where $\widetilde{T}$ is the analytical solution for a body in semi-infinite space, $\hat{T}$ is the complementary temperature field that is solved by the BVP numerically, and $\check{T}$ is the temperature field of specifically spaced image sources as the laser moves sufficiently near the part boundary [31,68,69].

In the process of the semi-analytical method for one layer, as described by Yang et al. [31], the scanning of the laser starts over the uppermost powder layer with a predefined scanning pattern and the increase in temperature within the body is solved by the BVP through FEA. This process is repeated until the entire part has been built. The assumptions of the problem are that the heat transfer between the solid and powder regions is negligible, as well as heat loss due to radiation and when compared to the heat transfer by conduction within the solid. In addition, the initial boundary condition is the current temperature of the body when the uppermost layer is placed, and the boundary condition is zero heat flux on the lateral and top surfaces of the body due to solid and powder interaction; whereas the boundary temperature at the bottom surface is that of the base plate. The melting, solidification, and phase change transformations are neglected with no loss of generality in predicting the thermal field [69].

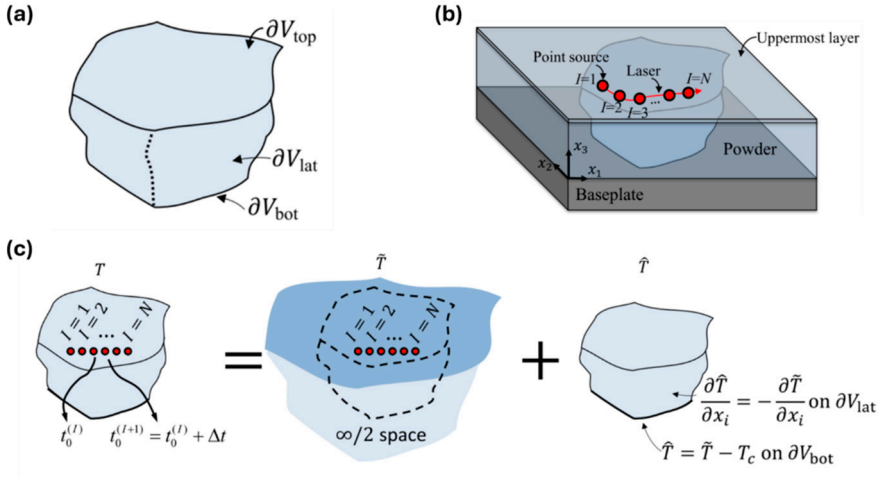

Figure 8. Schematic illustration of (**a**) the body V with its surface ∂V decomposed, (**b**) body V submerged into the powder bed bonded to the baseplate and the laser scan applied to the uppermost layer of the powder, and (**c**) decomposition of the thermal BVP (adapted from Yang et al. [31]).

To properly model the laser source movement, the mesh size of the FEA is discretized by a finite number of point sources that are separated by $v\Delta t$, where Δt is limited by the discretization of the FEA model and computational power available to effectively track the moving heat source. As a result, the mesh is typically kept sufficiently coarse well inside the part boundary. However, as the heat source approaches the boundary of the part, the mesh must be further refined to avoid deviation from the correct temperature solution [68]. This error in temperature is a direct result of $\hat{T}$ being negligible away from the part's edges so the part's temperature field is described by $\widetilde{T}$.

In another study, Cole et al. [66] developed a semi-analytical approach to solving the heat equation by using spectral graph theory and discrete Green's functions at various heating conditions in combinations of time and space. Whereas the previous semi-analytical method relies on intensive meshing and time integration steps typical of FEA processes, the application of graph theory allows for the meshless spatial relationships of temperature among discrete points, which simplifies thermal modeling. For the BVP, the Green's function solution, defined for the temperature, was defined as follows:

$$\widetilde{T}(\boldsymbol{r}, t) = \widetilde{T}_{in}(\boldsymbol{r}, t) + \widetilde{T}_{g}(\boldsymbol{r}, t) + \widetilde{T}_{bc}(\boldsymbol{r}, t) \tag{9}$$

where $\widetilde{T}_{in}$ is the temperature contribution from the initial condition, $\widetilde{T}_{g}$ is the temperature from internal heating, and $\widetilde{T}_{bc}$ is the temperature from the boundary conditions. An important aspect of the Green's function is to define the Laplacian matrix operator, which was derived using the concepts of numerical heat transfer and thermal resistances [70]. When demonstrating the utility of the developed semi-analytical method, Cole et al. [66] validated that the model agreed with experimental calibration and test case with absolute errors of less than 5%.

An application making the semi-analytical method useful for simulating the thermal field at the part scale was demonstrated by Moran et al. [68] with a V-22 osprey link. In this study, the complete part's thermal field was modeled and analyzed layer-by-layer to predict the distribution of thermal defects, namely lack of fusion defects and overheating, during the LPBF production of the part. The results successfully indicated the regions where the component is susceptible to defect formation, as shown in Figure 9a. However, the results are unable to identify the number of actual defects expected in the part, as no experimental validations for the part were performed. The defect thermal error index

values in Figure 9b indicate high probabilities of defects based on the temperature output threshold used in the study. While the semi-analytical method is able to model the laser movement well, it poses challenges to include the computational performance, and the amount of refinement needed to capture reasonable results [69]. With the amount of mesh refinement needed to properly capture the thermal field evolution for each layer scan of an entire part, it could take up to years in performing thermal analysis of the entire part, whereas the actual manufacturing time can take days. Therefore, a large cluster of computing power would be necessary to complete solutions at a reasonable time compared to the measure of fabrication time.

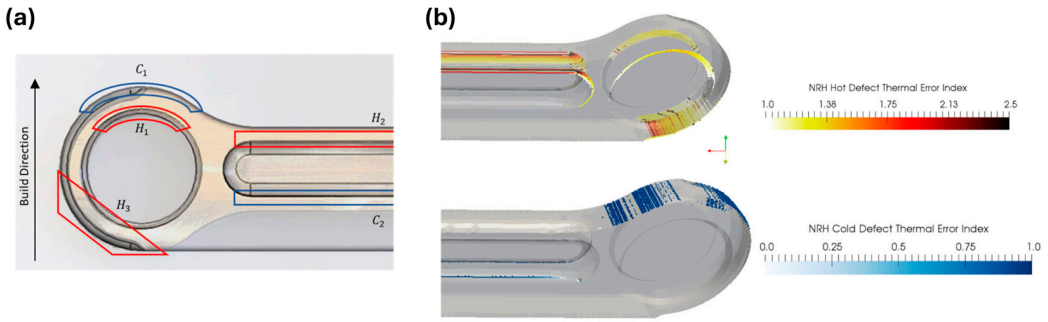

Figure 9. (**a**) Locations of hot and cold thermal error regions, respectively in red and blue, of the V-22 osprey link component and (**b**) spatial thermal error maps indicating hot and cold errors (adapted from Moran et al. [68]).

3.1.2. The Flash Heating Method

Unlike the semi-analytical method where the scanning pattern and single layers are analyzed, the flash heating (FH) method is also a part scale technique that analyzes full groups of layers at elevated temperatures to approximate the heating of individual laser scans [71]. The process of carrying out the simulation is to perform an analytical thermal loading for predetermined blocked layers (or meta-layers) of the component, determine the thermal gradients to a part scale model, and finally perform a structural simulation to predict the mechanical response to the applied thermal loads as the part is built. An important aspect of the FH method is that the thermal loading of the meta-layer is independent of laser-material interaction or, in other words, is independent of scan path, so an equivalent heat source is uniformly applied to the current activated meta-layer [67,72]. Depending on how thick the meta-layer is compared to an actual layer, the process input energy and volumetric energy applied is scaled proportionally by Δ/δ where Δ is the thickness of the meta-layer and δ is the actual layer thickness [67].

Williams et al. [73] applied the FH method to demonstrate the sequential application of the block deposition heated at the material melting temperature and allowed to cool transiently prior to the application of a new block, as shown in Figure 10. This entire process was repeated until the part was fully built. In their study, the vertical deflection of a bridge component due to warping as a result of part sectioning from the build plate was analyzed. When comparing the vertical deflection simulation results to the experiment, it was shown that results generally agree at the near zero position, where a leg was fixed to the build plate but diverged further along the span of the component (Figure 11). By varying the meta-layer height in the simulation build, the results show that larger block heights tend to diverge from the experimental measurements with underestimations near the zero x-position and overestimations for the max deflection at the end.

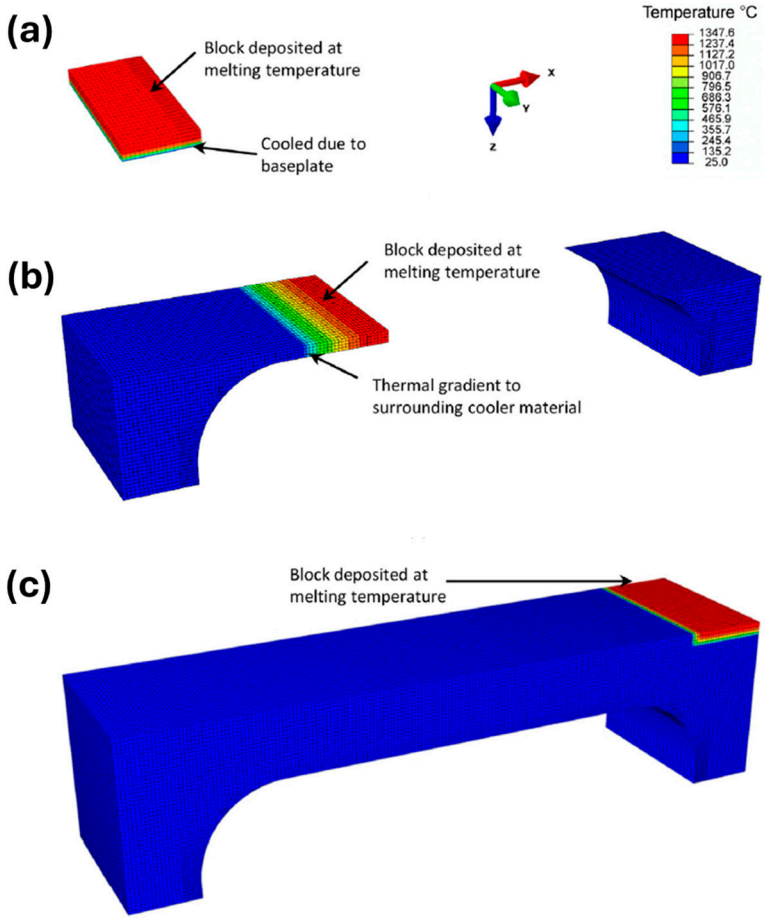

Figure 10. Sequence of the temperature evolution in the flash heating method for a bridge component with (**a**) the first deposited block, (**b**) a block deposited in the midsection of the build, and (**c**) the final block deposited completing the build [73].

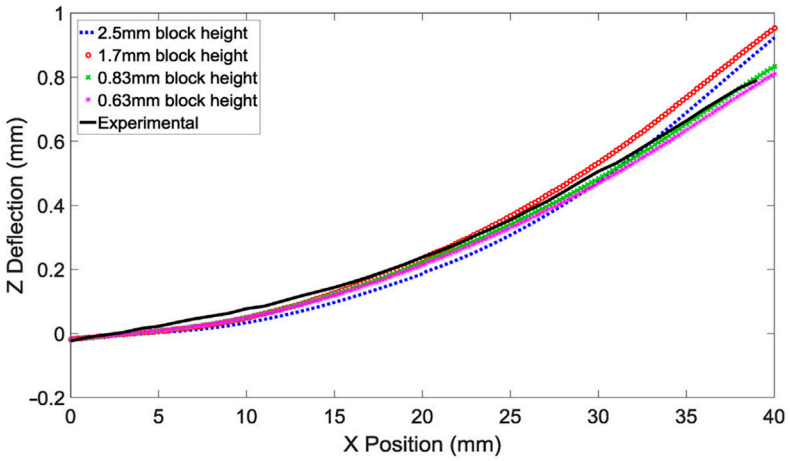

Figure 11. Vertical deflection of the bridge component due to sectioning off the build plate, with x = 0 as a fixed leg to the build plate and increasing x-values indicating removed sections [73].

3.1.3. The Agglomerated Heating Method

While the FH method is generally independent of the scan strategy through means of lumping multiple layers together, the agglomerated heating (AH) method [74] takes into account the laser pattern to simulate multiple physical layers. The detailed process simulation is carried out with agglomerated, or scaled, parameters of the powder layer thickness, laser radius, and laser power, keeping the scan speed constant. For example, Hodge et al. [75]

chose to scale their parameters to 20 physical layers, which translated to the laser beam profile in gray/black, as shown in Figure 12a, to be substantially larger than a typical laser diameter of about 50 µm [39] due to the chosen number of layers agglomerated.

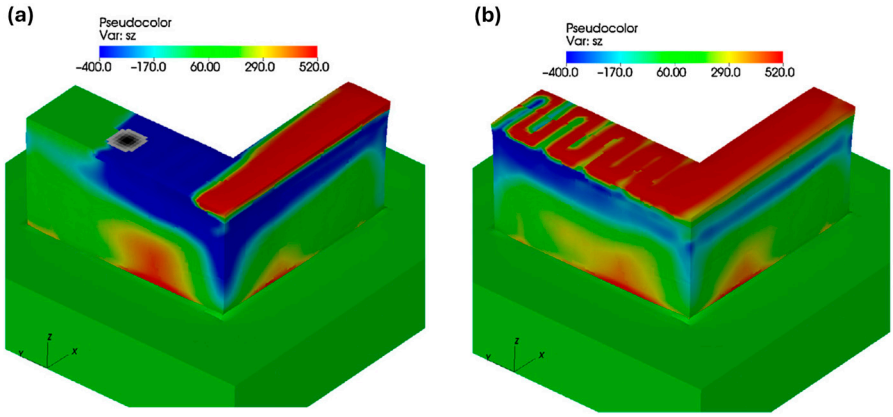

Figure 12. Sample scan of a layer in a L-shaped component (**a**) during and (**b**) after the laser scanning, where the gray/black circle indicates the laser beam at various time instances and color gradient represents the normal stress in the z-direction (adapted from Hodge et al. [75]).

The AH method, however, presents limitations in that the results are generally qualitative since the agglomerated layers are overheated due to the size of its laser source used in the model [74]. By overheating the layers, the thermal profile during the print is overestimated, thus the structural responses, such as stress and deformation, are overestimated [71]. Gouge et al. [71] reported that the simulations resulted in deformations that were 26–28% magnitude in error compared to experimental validations. In the LPBF process, the laser scan strategy, for example, plays a crucial role in accurately capturing the temperature changes that occur during the manufacturing process. The plastic deformation caused by the movement of the heat source is a significant factor contributing to the development of residual stresses developed in the component [35,76]. Understanding the relationship between the process parameters and the resulting residual stresses, as well as thermal deformation, is essential for improving the quality and performance of LPBF components.

3.2. Decoupled Thermomechanical Methods

Whereas the methods discussed in Section 3.1 are coupled with thermal–structural approaches, the methods presented in this section are decoupled, meaning that the part scale structural simulations do not entirely use the full thermal history of the part to predict residual stresses and thermal deformation.

3.2.1. The Inherent Strain Theory

The theory of inherent strains (IS) is fundamental to the concept of thermal cycling within welds [35]. Thermal cycling on welded objects causes repeated expansion and contraction which vary with time and location. Strains that appear in hot regions of welded areas are restrained by cooler regions further out because expansion is not uniform. When a new layer is added and heated in the LPBF process, the new material expands; however, it is constrained by the cooler part beneath, which results in compressive stresses in the new layer and tensile stresses below. Upon cooling, the new layer contracts faster than the lower part, generating tensile stresses in the new layer and compressive stresses in the cooler part underneath [77]. This local phenomenon results in plastic deformation and leads to residual stresses that are formed in the object after it cools to ambient temperatures; its associated strains are called inherent stresses. To introduce the IS, the total strain from

Equation (5) must include the effects of phase transformation and creep strain [35,78] and can be expressed as follows:

$$\boldsymbol{\varepsilon} = \boldsymbol{\varepsilon}_{el} + \boldsymbol{\varepsilon}_{p} + \boldsymbol{\varepsilon}_{th} + \boldsymbol{\varepsilon}_{pt} + \boldsymbol{\varepsilon}_{cr} \tag{10}$$

where the additional terms $\boldsymbol{\varepsilon}_{pt}$ and $\boldsymbol{\varepsilon}_{cr}$ are strains due to phase transformation and creep strain, respectively. Originally introduced by Ueda et al. [79,80], the inherent strain is defined by the difference of the total and elastic strains of a welded region at its cooled equilibrium state:

$$\boldsymbol{\varepsilon}^{*} = \boldsymbol{\varepsilon} - \boldsymbol{\varepsilon}_{el} = \boldsymbol{\varepsilon}_{p} + \boldsymbol{\varepsilon}_{th} + \boldsymbol{\varepsilon}_{pt} + \boldsymbol{\varepsilon}_{cr} \tag{11}$$

where $\boldsymbol{\varepsilon}^{*}$ denotes the inherent strain tensor.

The physical interpretation of the inherent strain is shown in Figure 13. Consider two material points A and B on the undeformed state of a small-scale solid to be at an initial distance of ds_0. After the welding process, the solid is stressed and the material points deform to new states A′B′ with a distance of ds due to induced thermal stresses. At this stressed state, the material is cooled down to a defined ambient temperature, causing thermal strains to relax. When cutting the material near the welded area, its stress is relieved causing mechanical elastic strain to be released and reach its stress-free state A″B″ at a distance ds^{*} [76].

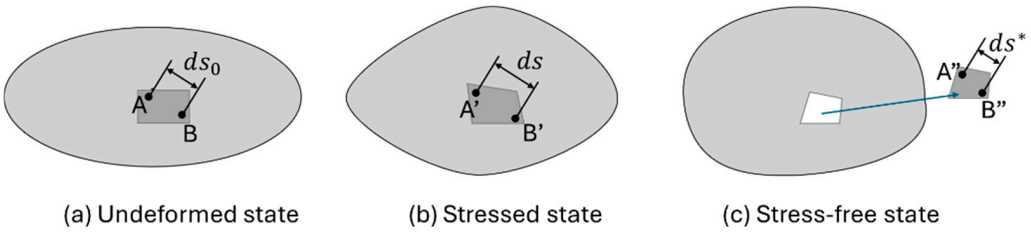

Figure 13. The original definition of inherent strains in welding processes.

In this process, the IS of an infinitesimal deformation is formulated from the undeformed state to the stress-free state as follows [76]:

$$\varepsilon^{*} = \frac{ds^{*} - ds_0}{ds_0} = \frac{ds - ds_0}{ds_0} - \frac{ds - ds^{*}}{ds_0} = \varepsilon - \varepsilon_{el} \tag{12}$$

where the inherent strain is the difference between the total strain experienced in the welding process and the elastic strain relaxation.

3.2.2. The Modified Inherent Strain Method

The original experimental method for determining inherent strains were performed with metal plates and assumed to be plastic strains only. However, this approach is inaccurate for metal AM processes due to their more complex physical phenomena compared to simple welding. Key deficiencies in the original IS theory to metal AM include treatment of welded material from the solid metal plate to powder bed particles, layer-by-layer shrinkage of upper layers that contribute to elastic deformation and stresses in lower layers, as well as a high dependence on boundary conditions and physical settings of the metal AM process that dictate inelastic strains [78]. Thus, the procedure for the modified IS method (MISM) was proposed to address the layer-by-layer nature of metal AM [76,78,81]. In this method, the inherent strain is taken as a process-history dependent quantity rather than being only dependent on the final cooled state. Since AM is a multilayer process, two major sources of IS are considered: contribution from plastic deformation, denoted as $\boldsymbol{\varepsilon}_{p}^{*}$, and contribution from thermal shrinking, coupled with an inter-layer effect, denoted as

ε^*_{th} [78]. In short, the mathematical presentation of the modified inherent strain model is summarized by:

$$\boldsymbol{\varepsilon}^* = \boldsymbol{\varepsilon}^*_p + \boldsymbol{\varepsilon}^*_{th} = \boldsymbol{\varepsilon}^I_p + \boldsymbol{\varepsilon}^I_e - \boldsymbol{\varepsilon}^S_e = \boldsymbol{\varepsilon}^I_{total} - \boldsymbol{\varepsilon}^S_e \quad (13)$$

where the MISM is defined by the difference in the total mechanical strain at the intermediate state, $\boldsymbol{\varepsilon}^I_{total}$ and the elastic strain at steady state, $\boldsymbol{\varepsilon}^S_e$ [76,81].

Implementation of the MISM takes two steps, as visualized in Figure 14. Under the representative volume detailed analysis, a microscale model of two layers ~1 to 10 mm in size is analyzed. A detailed thermal analysis is performed to obtain the thermal history, then a structural analysis is performed solving the continuity and stress equations to obtain and extract inherent strains [78,82], where the distortion energy theorem is typically used to determine when the solidifying material plastically deforms. Then, the assignment of the extracted IS value from the detailed analysis is applied as a constant to the whole component geometry using layer deposition modeling [83] to predict the resulting thermal distortion of the component.

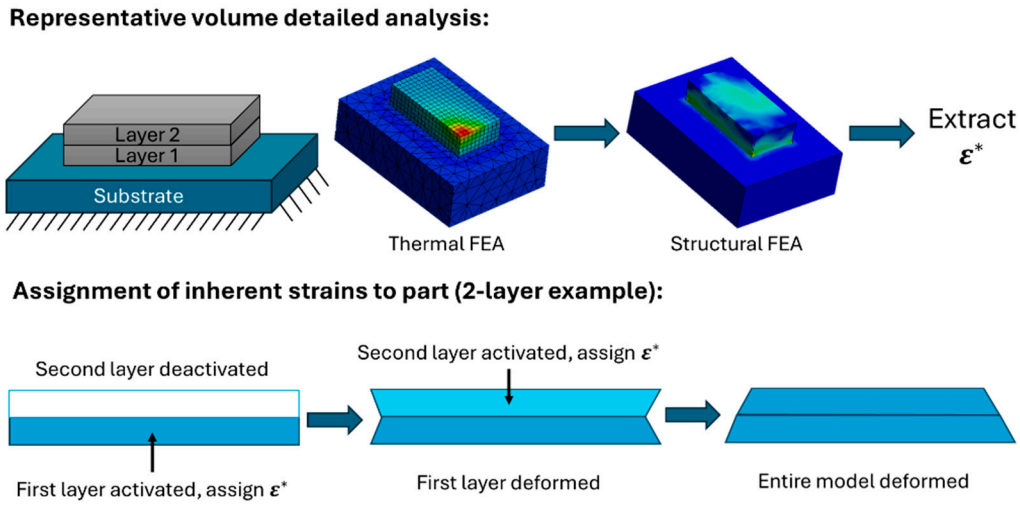

Figure 14. Summarized process of the modified inherent strain method.

3.2.3. Updates in the Modified Inherent Strain Methods

Since the original proposal of the MISM, new procedures and improvements to the method have been introduced. Dong et al. [82,84] found that the original procedure for implementing the MISM yielded inaccurate residual stress results due to only applying the IS at ambient temperature, resulting in an overestimation of elastic and plastic strains contributing to the total strain in the part scale. Instead of using constant ambient temperature material properties, the authors proposed a two-step process in which (1) the material properties at the intermediate temperature induce conversion of thermal strain to mechanical strain in the intermediate state and solve the equilibrium equation, then (2) adjust the material properties to those at the ambient temperature and solve the equilibrium equation again. In the work for predicting residual stress and distortion using the MISM [84], the model showed an increase in accuracy with errors for residual stresses from 46.5% to 8.7% for a 112 mm wall build and maximum distortion decreased from 29.7% to 7.9% for a 250 mm wall build. However, the authors reported a five-fold increase in computation time due to implementing a temperature dependent IS calculation, instead of keeping it constant.

It is important to note that the constitutive relationship used in the IS methods was assumed to be elastic–plastic, meaning the material curves are independent of strain rate. Bellet et al. [85,86] introduced the inherent strain rate method (ISRM) to calculate inherent

strains by using inherent strain rates. The ISRM assumes a thermo-elastic–viscoplastic constitutive model to perform analysis. Whereas the previous methods are dependent on the analysis of representative microscale models to inform the part scale, the ISR is updated as new layers are deposited through a live modeling reduction process. Mathematically, the total strain rate $\dot{\varepsilon}$ is presented as:

$$\dot{\varepsilon} = \dot{\varepsilon}^{el} + \dot{\varepsilon}^{vp} + \dot{\varepsilon}^{th} \tag{14}$$

where $\dot{\varepsilon}^{el}$ is the elastic strain rate, $\dot{\varepsilon}^{th}$ is the thermal strain rate, and $\dot{\varepsilon}^{vp}$ is the viscoplastic part of the strain rate [86,87]:

$$\dot{\varepsilon}^{vp} = \frac{3}{2\overline{\sigma}}\left[\frac{\overline{\sigma} - (\sigma_Y + R(\overline{\varepsilon}))}{k}\right]^{\frac{1}{m}} \boldsymbol{s} \tag{15}$$

where $\overline{\sigma}$ is the von Mises stress, σ_Y is the initial plastic yield stress, $R(\overline{\varepsilon})$ is the strain hardening function dependent on the generalized viscoplastic strain $\overline{\varepsilon}$, k is the viscoplastic constant, and m is the strain rate sensitivity constant. In the ISRM, the use of the viscoplastic term in the ISR calculation assumes time and temperature dependent creep in plastic deformation that the MISM does not account for [86]. While the authors showed this method to be accurate in predicting residual stress and distortion, there is a significant amount of time added in the computation time of this method when compared to the MISM. In addition, the works referenced do not provide experimental validation.

4. Modeling Software for Metal AM Processes

Simulation software, both commercial and research, serves a critical role in understanding the properties of AM components and thus, the technology itself. CAE software tools are sophisticated in handling the analysis of thermal, mechanical, and fluid dynamics as they apply to metal AM [88]. Of particular interest, CAE can be used to analyze heat flow and mechanical system deformation to investigate the development of residual stresses caused by thermal and mechanical loading [16].

Active areas of research for software tools include process modeling of the microstructure evolution during solidification and grain growth [89–91] and distortion and stresses in components. Multiscale simulation is increasingly becoming critical to achieve a comprehensive understanding of the entire metal AM process [20,22,27,92–94]. However, this is difficult to accomplish with today's computational power. Simulation and analysis through methods, such as FEA and computational fluid dynamics (CFD), have been used over several decades to model various physical phenomena. A list of commercial software that integrates AM processes in their FEA codes is shown in Table 2, where its capabilities for analysis, physics incorporated, method of analysis, and analysis scales are briefly summarized.

With respect to the modeling methods discussed in the previous section, the FEA software listed traditionally tend to follow a coupled thermomechanical analysis, where the thermal analysis precedes the structural analysis, which is seen in such works produced by Chen et al. [81], using ANSYS, and Mollamahmutoglu et al. [95], using COMSOL. However, Ninpetch et al. [96] used Simufact to model the MISM without the need of performing and obtaining the thermal history and purely modeled the additive nature of LPBF, as depicted in Figure 14.

Table 2. Commercial FEA software available to simulate AM processes.

Software	Website	Capabilities	Physics for AM	Method of Analysis	Scales of Analysis
ANSYS Additive Suite (3DSim)	https://www.ansys.com/products/additive (accessed on 1 August 2024)	Design, optimization, build thermal and static analysis Additive Science: melt pool, scan strategy, microstructure models	Thermal model: heat transfer equation Structural: equilibrium	Thermal model: flash heating method Structural: inherent strain method	Multiscale: microstructure, melt pool, thermal layer history, part-scale distortion, and residual stress
Autodesk Netfabb	https://www.autodesk.com/products/netfabb/overview (accessed on 1 August 2024)	Creation of process parameter files to run macroscale simulations	Thermal: energy balance, Goldak's ellipsoid heat source model Structural: equilibrium	Thermal model: detailed microscale process Structural: inherent strain method (uniform strain)	Multiscale: Detailed fine-scale process parameter model, part-scale geometric model
COMSOL Multiphysics	https://www.comsol.com/ (accessed on 1 August 2024)	Multiscale physics phenomena that can be completed simultaneously	Heat transfer, multiphase fluid flow	Coupled fluid flow and heat transfer	Microscale: melt pool
Simufact Additive	https://www.simufact.com/simufact-additive.html (accessed on 1 August 2024)	Part scale distortion, residual stress, build space, optimization, manufacturing issues, postprocessing	Thermal: energy balance Structural: equilibrium	Thermal method not disclosed Inherent strain method Coupled thermo-mechanical calculation method	Part scale only
Siemens NX-AM	https://www.plm.automation.siemens.com/global/en/products/manufacturing-planning/additive-manufacturing.html (accessed on 1 August 2024)	Design, optimization, build part preparation, build simulation, machine connectivity export	Thermal: energy balance Structural: equilibrium	Thermal model: flash heating method Structural: inherent strain method (uniform strain)	Part scale only
Altair Amphyon (Additive Works)	https://www.oqton.com/amphyon/ (accessed on 1 August 2024)	Build thermal and structural analysis, compensated part distortion, build orientation determination	Thermal: energy balance Structural: equilibrium	Thermal model: flash heating method Structural: inherent strain method	Part scale only

While FEA has capabilities in performing simulations of varying scales, it is mostly useful in elucidating properties in the part scale, due to the necessary simplifications required to numerically solve complex physics in the formation of the finite element equations. A key issue is choosing the appropriate representation of the heat sources [35] and associated physical phenomena [97], which could result in an overestimation of the temperature field of printed components. To combat this, CFD has been used to incorporate more complex physics, as described in Section 2.1. Namely, mechanisms related to metal vaporization that influence other phenomena related to melt pool formation are incorporated for the LPBF process [98,99]. Table 3 provides a list of commercial and research codes available to model and simulate melt pool processes in metal AM.

Table 3. Commercial CFD software available to simulate AM processes.

Software	Website	Capabilities	Physics for AM	Method of Analysis	Scales of Analysis
FLOW-3D AM	https://www.flow3d.com/products/flow3d-am/ (accessed on 1 August 2024)	CFD for multiple AM processes: LPBF, direct energy deposition, binder jetting, fused deposition modeling	Heat transfer, particle spreading, melting, multilayer analysis, keyholing, scan strategy, beam shaping, multi-material PBF	Free surface fluid flow, volume of fluid method	Microscale: powder bed level
ANSYS Fluent	https://www.ansys.com/products/fluids/ansys-fluent (accessed on 1 August 2024)	General CFD problems, although not set up properly to handle AM-specific problems	Thermal history: solidification, melting Source terms in energy and momentum: Buoyancy, Marangoni effects, phase changes	Volume of fluid method	Microscale: melt pool
ALE3D (LLNL)	https://ale3d4i.llnl.gov/ (accessed on 1 August 2024)	CFD, solves and simulates various flow problems	Laser energy deposition, heat transfer, surface tension, vapor recoil	Coupled fluid flow and heat transfer using arbitrary Lagrangian–Eulerian techniques	Microscale: powder bed level, melt pool
OpenFOAM (University of Erlangen–Nuremberg)	https://www.openfoam.com/ (accessed on 1 August 2024)	Open source CFD for many applications, text-based simulation (no GUI)	Heat transfer, multiphase flows, thermophysical models	Volume of fluid method	Microscale: melt pool, powder bed

4.1. Part Scale LPBF Modeling and Simulation Using FEA

In Section 3, various thermomechanical models discussed use FEA to obtain part scale thermal and structural predictions. The basic concept of applying the finite element method is to consider a structure discretized as simple elements connected at their nodes and solve weak form representations of partial differential equations to obtain approximate solutions [100]. For thermal FEA, Equation (7) is solved with initial conditions for a new powder layer [101]:

$$T(x, y, z, t_0) = T_0 \tag{16}$$

where (x, y, z) is the location of the new layer, t_0 is the time step in which the new layer is applied, and T_0 is the temperature of the new layer. The general boundary conditions associated with thermal FEA problem are as follows [102]:

$$-k\nabla T \cdot \boldsymbol{n} = h(T - T_0) + \xi\sigma_{SB}\left(T^4 - T_0^4\right) + \overline{q} \tag{17}$$

On the left-hand side of Equation (16), $\boldsymbol{n}$ signifies the normal vector to the surface in which the condition is applied. On the right-hand side of the equation, the first term is the convective heat loss, where h is the heat transfer coefficient, the second term is the heat loss due to radiation where ξ is the emissivity of the material and σ_{SB} is the Steffan–Boltzmann constant, and the third term $\overline{q}$ rate of heat input from the laser source.

For structural FEA, the static equilibrium equation, as shown in Equation (17), is solved [102].

$$\nabla \cdot \boldsymbol{\sigma} = 0 \tag{18}$$

The associated displacement boundary condition is given by

$$\boldsymbol{u} = \overline{u} \tag{19}$$

where $\boldsymbol{u}$ is the displacement vector and $\overline{u}$ is usually set to zero because the entire part is fixed to the build plate, with no external body or traction forces that cause relative motion during the LPBF process.

While FEA is able to elucidate the multiscale aspects of the LPBF process, there remain active areas of research to address computational challenges as well as the fidelity of the analyses completed. For example, ANSYS offers two comprehensive AM platforms, which provide designers with the tools to analyze the process, materials, and component validation in the context of design for AM (DfAM) [103]. The simulation approaches taken by ANSYS are through a simplified approach using the Additive Print (AAP) software (per v2021) and a fully embedded environment within Workbench, called Additive Suite (AAS). When using AAP, a constant inherent strain value is a priori assumed to perform fast simulations and are user inputs by:

$$\varepsilon^* = SSF \cdot \frac{\sigma_Y}{E} \tag{20}$$

where SSF is the isotropic strain scaling factor and E is the material's elastic modulus, which are dependent on the calibration of print geometries and independent of a thermal analysis [103,104]. For anisotropic analysis, an additional factor called the anisotropic strain coefficients (ASC) are multiplied to Equation (20) to account for the scan pattern. In addition, it is assumed that the inherent strain is applied at the yield strength. The yielding condition in structural FEA is given by [87]:

$$\sigma - \sigma_Y \leq 0 \tag{21}$$

When this condition is met and the component experiences stresses beyond its yield stress limit, the component in consideration is no longer elastic deformation, but entering a permanent or plastic form of deformation. Due to the high temperatures experienced in the LPBF process, this is to be expected [52]. To account for plasticity, constitutive models, such as those described in Section 3.2 for the IS methods, are numerically implemented [87].

For AAS, a coupled simulation in Workbench is performed where a transient thermal calculation is performed prior to a static structural simulation [105]. In this modeling technique, the numerical layers in the FEA represent agglomerated layers and are sequentially activated using the element birth and death method [83] and is heated akin the FH method to perform analysis. Within Workbench, ANSYS has integrated the AM process steps to show how the simulation is performed overall, as shown in Figure 15. Under the static structural simulation, there is an option to perform additional steps in the process, including heat treatment and support structure removal [105].

In the comparative study produced by Mayer et al. [103], they concluded that the simulation approaches offered by ANSYS present good qualitative predictions for the parts that were investigated. While AAS can perform more advanced process simulations in comparison to AAP, the dependence on data generation is required for both platforms to achieve accurate results. This implies that a large amount of calibration from physical geometries and scanning strategies are necessary to substantiate the predictive models. To further elucidate the capabilities of the ANSYS AM platforms, Weber et al. [106] also observed that thermal properties for LPBF powder materials are not often available, resulting in additional deviations from simulations and actual experiments.

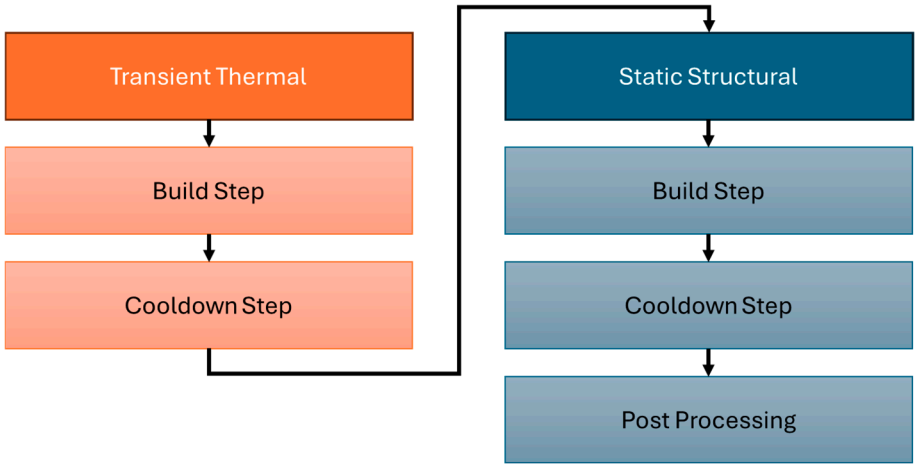

Figure 15. Summarized sequential steps taken in ANSYS Additive Suite to perform AM simulations.

4.2. Melt Pool Scale Modeling and Simulation Using CFD

One disadvantage of using FEA to model and simulate the LPBF process is that it does not fully capture the full complexity of the physics at the melt pool scale. Several assumptions and simplifications must be made to perform analysis with the available computing resources and limitations of FEA [107]. In an effort to correlate melt pool properties to the LPBF process parameters, Vanini et al. [108] developed an FEA model that captures melt pool morphology. However, this model is limited in its study when considering thermal deformations, only providing a qualitative treatment based on their experimental results. Unlike FEA, CFD simulations are able to model the deformation that occurs within fluid systems. Since the material melted in LPBF go through multiple phase changes, from its powder particle form to liquid that coalesces as the melt pool then to final solid of the part being manufactured [36], understanding how the material deforms and influences the part build at the powder scale can be useful in analysis. While the literature has often neglected to consider the thermo-fluid dynamics (TFD) [109] due to added complexity, it does aid in predicting and analyzing melt pool evolution and microstructural growth [55,109,110]. Additionally, forces of TFD, such as the Marangoni forces that drive mixing within the melt pool, contribute to reducing the overestimation of peak temperature and shape of the melt pool seen in models based on heat conduction only. This was observed by Mukherjee et al. [97], where the conduction-only model produces a 400 K difference in peak temperature and a narrower temperature distribution in comparison to the conduction and convection model used, as shown in Figure 16. Thus, inaccurate temperature distributions can have negative impacts on the energy delivered to the melt pool, leading to unrealistically high cooling rates [110], which impacts predictive results of stress and strain distributions during fabrication [111].

A popular commercial CFD software, FLOW-3D [112], was developed to model the LPBF process at the powder scale and has been used by many researchers to study areas in melt pool dynamics to thermal gradients developed that influence more macroscale material properties [111,113–117]. The process in which FLOW-3D is able to describe the TFD of the melt pool is through the volume of fluid method [118,119] where, in addition to solving the conservation equations Equation (1) through (3), it solves the free surface of the working fluid equation.

$$\frac{\partial F}{\partial t} + \nabla \cdot (F\boldsymbol{v}) = 0 \tag{22}$$

Here, F denotes the fluid fraction within a CFD cell and is used for reconstructing the free surface of the melt pool at a time increment. When comparing the results of CFD simulation to obtain thermal history to that of a thermomechanical simulation performed

in FEA, the CFD-based simulations closely mimic the evolution of the free surface of actual melt pools, as shown in Figure 17. In addition, the profiles of the melt pool and stress distributions in the CFD simulations show a more irregular gradient than the FEA based counterparts. This suggests that a high-fidelity model can be used to accurately predict potential areas of high stresses and defects during the LPBF manufacturing process [111].

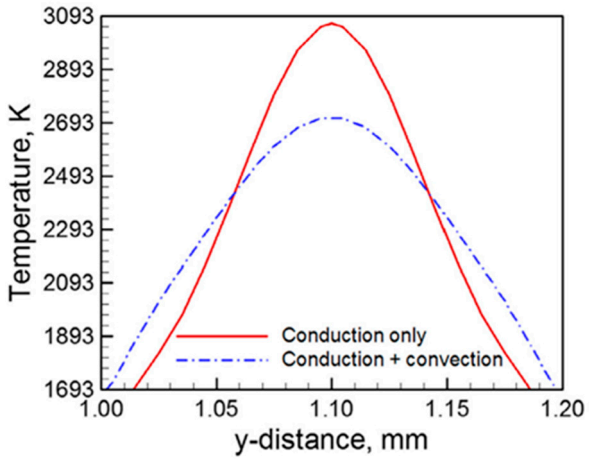

Figure 16. Comparison in models of the temperature variation inside a melt pool near the laser beam source [97].

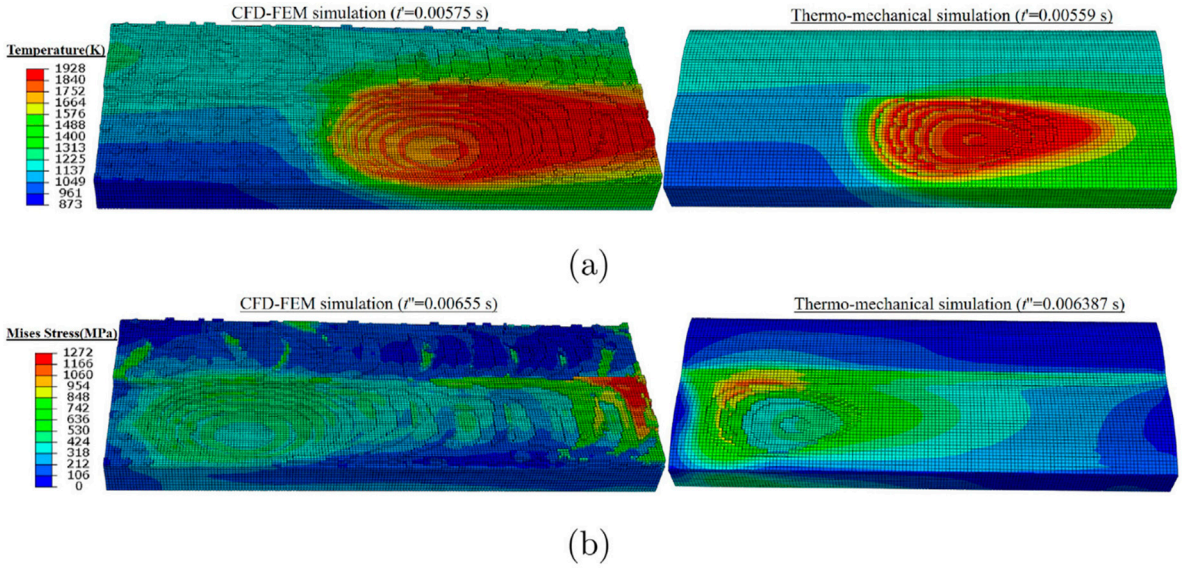

Figure 17. Comparison of the (**a**) temperature and (**b**) stress distribution profiles for CFD-based and FEA-based simulations [111].

5. Qualification Processes of LPBF Components

In the past few years, standards related to the certification process of metal AM have been developed. Still, a major challenge lies in the protocols in which many industries utilize the technology. For example, in the aerospace industry, metal AM built components must pass the rigorous certification process to adopt parts into major systems [4,120]. However, due to lack of prior knowledge and traceability of the AM process, not to mention industries adopting the technology for the first time, it is difficult to provide detailed and complete verification and validation studies of metal AM material properties that are unified [4,12,120]. Work detailing the characterization of materials and failure mechanisms are essential when demonstrating an AM part's ability to perform equivalently or better than its traditionally manufactured counterpart.

Rigorous standards are needed to alleviate many of the problems concerning inconsistent methods, including testing, process checks, quality, and evaluation of materials [4,12]. Currently, organizations such as ISO/ASTM and SAE have developed a wide range of standards that encompass the elements, as shown in Figure 18, which make the adoption of metal AM traceable and can accommodate a more streamlined process in ensuring metal AM is appropriate for various industries [13]. A summary of several commercial standards specifically for LPBF are shown in Table 4. Current standards assume metal AM to be a high-risk technology, so substantiation of the entire fabrication process from material selection, machine set parameters, and its resulting material properties, as well as machine/facility requirements, must be provided to achieve qualification and acceptance.

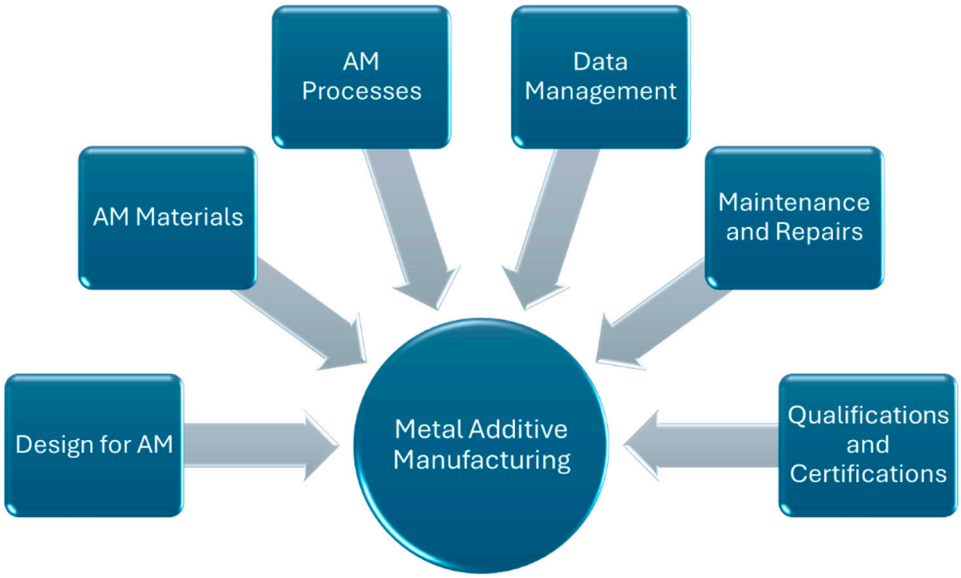

Figure 18. Overview of standards required for a comprehensive metal AM technological adoption.

Achieving a totally qualified part utilizing AM requires a compliance strategy. A combination of physics-based modeling as well as experimental verification and validation early in the design process for an AM component can help alleviate any inevitable inflexibilities in decision-making further as more knowledge is gained about the product through time [121]. An example of a compliance strategy through a certification framework is shown in Figure 19, where the enclosed gray box utilizes an integrated computational material engineering (ICME) platform presented by Megahed et al. [38]. The framework sequentially outlines the process of how performance of a component is assessed. The evaluation comprises modeling both the powder material and the component to be used in the manufacturing process. Computational models were used to study the effects of input process parameters during material development and process qualification stages. Furthermore, the authors performed a case study of a rocket nozzle where a distortion and residual stress model was used to predict the final shape of the component as well as critical features on the part. The model was able to predict material strength and accuracy of the design through target metrics by using the qualification framework, when compared to experimental assessments.

In an effort to centralize the qualification process framework, Dordlofva [122] proposed a design for qualification framework using six design tactics, as shown in Figure 20. Rather than holistically looking at the functions of the AM technology to produce a qualified part through the common viewpoint of DfAM [4,88,120], the proposed framework supports the engineering process by proactively considering the qualification process during AM component development. The framework emphasizes the need for early consideration of

the qualification requirements during the design process, relying on AM process knowledge to capture requirements ensuring parts can be qualified in a verification approach. In the six tactics shown in Figure 20, the process outlined is highly part dependent, which insinuates that the road to qualification is part specific since the system need, requirements, and verification plan rely on the application itself more than the AM technology used to produce the part.

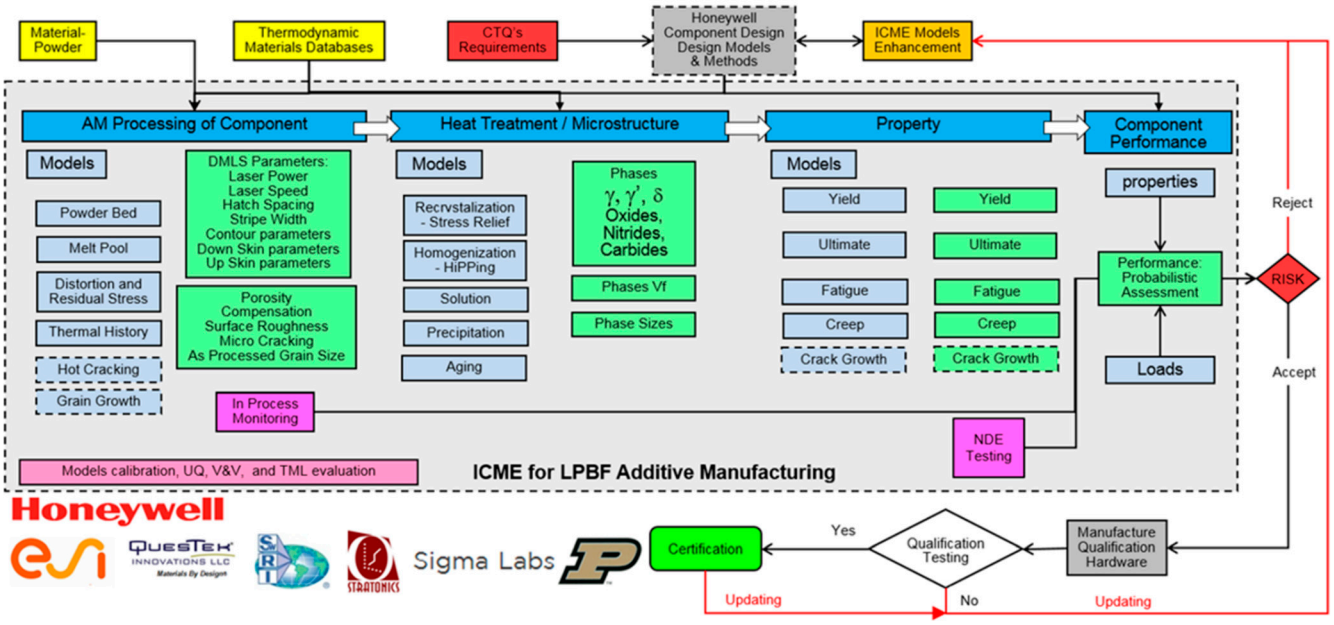

Figure 19. A certification framework for qualifying metal AM components [38].

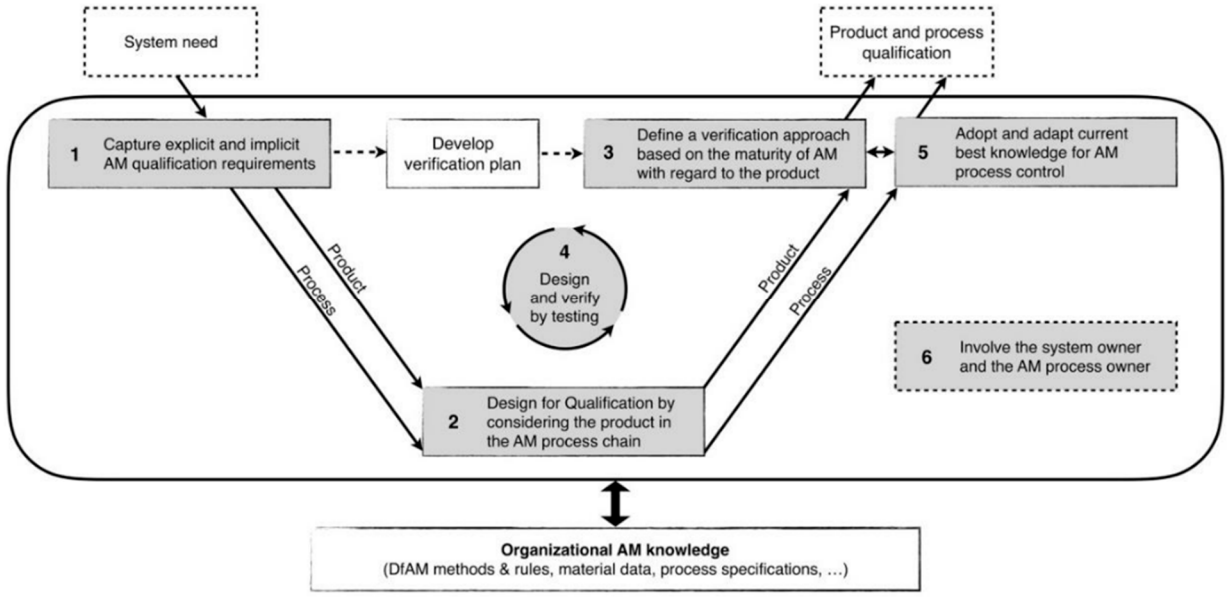

Figure 20. The proposed design for qualification framework [122].

Whereas the frameworks aforementioned provide a good outline for part and process acceptance of the LPBF process, the qualification process must be substantiated and compliant to standards identified by its users. In the context of process verification, the design freedom of the LPBF process relies mostly on material curves obtained through experimental testing, such as ASTM E8 tensile bars [123]. Factors such as component features, performance requirements, material limitations, and criticality significantly influence the application of LPBF [124]. ASTM 52902 can be used as a benchmark, outlining

the qualification of process development and validation to ensure part accuracy and desired material properties. The design of components, however, is dictated by the loading conditions the part is subjected to [122]. To enable successful integration of metal AM processes, thorough requirements research must be performed [12]. A consideration of factors, such as part complexity, size, alloy selection, potential failure modes, and component performance metrics, must be identified early in the design process. By aligning with established standards, the design approach taken in the qualification process can address the challenges and opportunities presented by the LPBF process, enabling the production of reliable, high-performance components [4].

Table 4. Commercial standards and requirements developed for metal AM LPBF [125–146].

Specification	Title/Scope
ISO/ASTM 52900	Additive manufacturing—General principles—Fundamentals and vocabulary
ISO/ASTM 52901	Requirements for purchased AM parts
ISO/ASTM 52902	Additive manufacturing—Test artifacts—Geometric capability assessment of additive manufacturing systems
ISO/ASTM 52904	Practice for metal powder bed fusion process to meet critical applications
ISO/ASTM 52905-EB	Non-destructive testing and evaluation—Defect detection in parts
ISO/ASTM 52908-23	Post-processing, inspection and testing of parts produced by powder bed fusion
ISO/ASTM 52920-23	Requirements for industrial additive manufacturing processes and production sites
ISO/ASTM 52930-21	Installation, operation and performance (IQ/OQ/PQ) of PBF-LB equipment
ISO/ASTM 52941-210	Acceptance tests for laser metal powder-bed fusion machines for metallic materials for aerospace application
ISO/ASTM 52942-20	Qualifying machine operators of laser metal powder bed fusion machines and equipment used in aerospace applications
ISO/ASTM 52950-21	Additive manufacturing—General principles—Overview of data processing
ASTM F3530-22	Post-Processing for Metal PBF-LB
ASTM F3572-22	Part Classifications for Additive Manufactured Parts Used in Aviation
ASTM F3592-23	Standard Guide for Additive Manufacturing of Metals—Powder Bed Fusion—Guidelines for Feedstock Re-use and Sampling Strategies
ASTM F3626-23	Accelerated Build Quality Assurance for Laser Beam Powder Bed Fusion (PBF-LB)
SAE/AMS 7003	Laser Powder Bed Fusion Process
SAE/AMS 7032	Machine Qualification for Fusion-Based Metal Additive Manufacturing
SAE/AMS 7002A	Process Requirements for Production of Metal Powder Feedstock for Use in Additive Manufacturing of Aerospace Parts
AWS D20.1	Specification for Fabrication of Metal Components Using Additive Manufacturing
SAE/AIR 7352	Additively Manufactured Component Substantiation
DIN 65123	Aerospace series—Methods for inspection of metallic components, produced with additive powder bed fusion processes
DIN 65124	Aerospace series—Technical specifications for additive manufacturing of metallic materials with the powder bed process

6. Discussion

The role of modeling the physical effects within the LPBF process must be studied carefully, as it is essential to obtain quality and reliable parts. To our knowledge, there is no one unified solution to this problem, as many researchers and industries alike approach modeling techniques differently. An important issue to recognize is the vast scale on which the LPBF process must be modeled and the computational resources available. For

example, performing a full CFD analysis of an entire part build is infeasible due to many computational limitations, such as the number of iterations required to solve a single timestep of a single melt pool evolution. Chen and Yan [111] reported that using CFD to complete a thermal-fluid simulation took 700 h, compared to an FEA simulation that took 330 h to complete for a two-line single layer pass travelling only 2.14 mm on the computational domain. While there is an increase in fidelity of the complex physics of the melt pool, it is unrealistic to incorporate a full part analysis using CFD where parts can be upwards of 100 cm. On the other hand, completely relying on a part scale analysis to accurately predict residual stress and thermal distortion of components have, at best, been qualitative due to simplifications in the thermal simulation process [103]. Even with the advancement and improvement of methods discussed above, a large amount of data gathering of more complex geometries are required to gain further understanding of the parts manufactured by the LPBF process. Thus, an opportunity for future development in modeling physical phenomena within the LPBF process would be to investigate critical features of components along with their corresponding processing parameters. Such an investigation would lead to a better understanding of how they influence resulting temperature distributions, microstructure, strength properties, and quality of the final manufactured components.

In addition, it is evident that performing a multiscale simulation is a difficult problem to solve. In order to build such a framework, a tradeoff in simulation accuracy and computational feasibility between melt pool dynamics, part scale residual stress, and thermal distortion would be essential. Currently, thermomechanical models use simplified thermal models due to the complex phenomena in the melt pool and capturing that in the part scale is impracticable. Bresson et al. [92] proposed a multiscale method that could be used to bridge the gap between temporal and spatial differences in modeling techniques by using FEA. While the proposed simulation method aimed at zooming down from part scale to the melt pool, it was specified that the user must make a choice for what specific areas within the part must be zoomed into because of computational limitations. Despite this, a framework to build an integrated multiscale system is possible, and it is worth investigating such a comprehensive system. A future research direction in LPBF simulations is not only to enhance computational methods, but to develop computationally viable simulations that enable the use of high-fidelity models. These models should utilize resources, such as high-performance computing, to reduce computation time, while obtaining reliable results.

With respect to the qualification of the LPBF process, candidate components must achieve equivalent or better performance than their traditionally manufactured counterparts to ensure they can be reliable substitutes. This can be achieved through computational modeling and simulations to predict essential properties and can inform us how process parameters, post heat treatment, and material properties are set for AM materials. Of course, experimental validation needs to occur to ensure the processes and established guidelines for manufacturing are repeatable. Frameworks such as the ones shown in Figures 19 and 20 provide a good path towards developing strategies for the adoption of metal AM as a leading manufacturing method to support the acquisition of components where diminishing sources exist [120]. As a potential research path, a framework geared towards process qualification within a virtual integrated tool environment would be cost effective when considering adoption of the LPBF process in place of traditional manufacturing methods. When based off historical part and system data, the qualification framework would ensure the accuracy and reliability of the LPBF process for its adoption in major manufactured systems through validated modeling and simulations.

7. Conclusions

The modeling and simulation of the metal AM LPBF method is complex, as it spans multiple length and time scales. In the microscale, analysis involves the study of the melt pool from thermal field evolution to microstructure development dependent from thermal gradients. The analysis at this scale typically covers the length of micrometers with a time span of microseconds, which results in fine time steps to accurately capture the physics occurring at this scale. Depending on the computing power, simulations can take from hours to days to solve, assuming the simulation is set up correctly. On the other hand, macroscale analysis involves the study of multiple layers to a complete part build where the length scale is typically centimeters to meters. Depending on the size of the components being analyzed, the time scale being analyzed covers build times of many hours. As seen above, part scale analysis can be achieved in minutes to hours to obtain residual stress and thermal deformation measurements. Since there is a vast difference in solution times, a complete multiscale analysis cannot be completed for a component manufactured via the LPBF process with today's computing power due to the complexities seen with microscale analysis.

While progress has been made in developing the elementary understanding of the LPBF process, the relationship of process parameters impacting melt pool characteristics and the final build of the parts still require further study. Various modeling and simulation techniques, as discussed above, have been explored and show capabilities in being able to accurately predict the material properties of metal AM components. Being able to predict these properties firsthand through modeling and simulation can reduce the cost of the part manufacturing, since physical materials testing, manpower, and time are reduced. In addition, early modeling and simulation can inform further design decisions, such as post-treatment of as-built properties, to reduce the effects of defects inherent in the manufacturing process. This can largely influence the final quality of the parts being manufactured.

To achieve accurate builds and repeatable components, the metal AM technology depends on standardized practices. While published standards for the LPBF process are necessary and detail essential substantiation requirements, they do not specifically address the quantitative measures that are explicit to changing the processes and unique parts produced. An additional or modified approach to the qualification processes and standards must be developed to address these gaps. While the capabilities of metal AM are still being understood, as the field continues to grow, it introduces additional challenges that must be addressed through additional innovations so a deeper, more comprehensive knowledge base can be achieved. Through advancements in modeling and simulations, users of metal AM are able to develop and produce critical information to adopt the technology as an essential part of their supply chains and continue to support sustainment issues surrounding older systems.

A summary of challenges and future directions for research discussed in this work are summarized below:

- To address issues in understanding physical phenomena in the LPBF process, a focus on critical component features and corresponding processing parameters can lead to an enhanced understanding of the resulting properties of components.
- To improve capabilities in current modeling and simulation methods, future research should be focused on enabling high-fidelity LPBF models through high-performance computing to reduce computation time and obtain reliable results.
- To adopt the LPBF process as a reliable manufacturing method, an investigation of a qualification framework utilizing a cost-effective virtual integrated tool environment should be assessed to evaluate capabilities in producing accurate and reliable components.

Author Contributions: Conceptualization, E.D.L. and Y.L.; writing—original draft preparation, E.D.L.; writing—review and editing, A.R., B.D.B., C.B., Z.S. and Y.L.; supervision, Y.L.; funding acquisition, Y.L. All authors have read and agreed to the published version of the manuscript.

Funding: This research was funded by the Air Force Research Laboratory, grant number FA8650-23-C-5701, project manager: Mark Benedict. The authors have also received research support from the Oklahoma Aerospace and Defense Innovation Institute at the University of Oklahoma.

Data Availability Statement: No new data were created.

Acknowledgments: Financial support was provided by the University of Oklahoma Libraries' Open Access Fund. E.D.L. would also like to acknowledge the SMART Scholarship Program for providing educational support toward the completion of his Ph.D. work.

Conflicts of Interest: The authors declare no conflicts of interest.

References

1. Langnau, L. US Air Force and GE Reach First Metal Additive Technology Milestone with Sump Cover for F110 Engine. Available online: https://www.engineering.com/us-air-force-and-ge-reach-first-metal-additive-technology-milestone-with-sump-cover-for-f110-engine/ (accessed on 1 September 2024).
2. Kennedy, R. Outside the Box: How GE Aviation Entered the Brave New World of Additive Manufacturing. Available online: https://www.geaerospace.com/news/articles/100-year-anniversary-manufacturing-technology/outside-box-how-ge-aviation-entered-brave (accessed on 1 September 2024).
3. Sames, W.J.; List, F.A.; Pannala, S.; Dehoff, R.R.; Babu, S.S. The metallurgy and processing science of metal additive manufacturing. *Int. Mater. Rev.* **2016**, *61*, 315–360. [CrossRef]
4. Blakey-Milner, B.; Gradl, P.; Snedden, G.; Brooks, M.; Pitot, J.; Lopez, E.; Leary, M.; Berto, F.; du Plessis, A. Metal additive manufacturing in aerospace: A review. *Mater. Des.* **2021**, *209*, 110008. [CrossRef]
5. Smith, J.; Xiong, W.; Yan, W.; Lin, S.; Cheng, P.; Kafka, O.L.; Wagner, G.J.; Cao, J.; Liu, W.K. Linking process, structure, property, and performance for metal-based additive manufacturing: Computational approaches with experimental support. *Comput. Mech.* **2016**, *57*, 583–610. [CrossRef]
6. Joshi, S.; Martukanitz, R.P.; Nassar, A.R.; Michaleris, P. *Additive Manufacturing with Metals*; Springer Nature: Cham, Switzeland, 2023.
7. Bergmueller, S.; Gerhold, L.; Fuchs, L.; Kaserer, L.; Leichtfried, G. Systematic approach to process parameter optimization for laser powder bed fusion of low-alloy steel based on melting modes. *Int. J. Adv. Manuf. Technol.* **2023**, *126*, 4385–4398. [CrossRef]
8. Li, C.; Liu, J.F.; Guo, Y.B. Prediction of Residual Stress and Part Distortion in Selective Laser Melting. *Procedia CIRP* **2016**, *45*, 171–174. [CrossRef]
9. Ki, H.; Mazumder, J.; Mohanty, P.S. Modeling of laser keyhole welding: Part I. mathematical modeling, numerical methodology, role of recoil pressure, multiple reflections, and free surface evolution. *Metall. Mater. Trans. A* **2002**, *33*, 1817–1830. [CrossRef]
10. Hagenlocher, C.; O'Toole, P.; Xu, W.; Brandt, M.; Easton, M.; Molotnikov, A. Analytical modelling of heat accumulation in laser based additive manufacturing processes of metals. *Addit. Manuf.* **2022**, *60*, 103263. [CrossRef]
11. Gouge, M.; Michaleris, P. *Thermo-Mechanical Modeling of Additive Manufacturing*; Gouge, M., Michaleris, P., Eds.; Elsevier: Amsterdam, The Netherlands, 2018.
12. Gradl, P.; Tinker, D.C.; Park, A.; Mireles, O.R.; Garcia, M.; Wilkerson, R.; McKinney, C. Robust Metal Additive Manufacturing Process Selection and Development for Aerospace Components. *J. Mater. Eng. Perform.* **2022**, *31*, 6013–6044. [CrossRef]
13. Chen, Z.; Han, C.; Gao, M.; Kandukuri, S.Y.; Zhou, K. A review on qualification and certification for metal additive manufacturing. *Virtual Phys. Prototyp.* **2021**, *17*, 382–405. [CrossRef]
14. DebRoy, T.; Wei, H.L.; Zuback, J.S.; Mukherjee, T.; Elmer, J.W.; Milewski, J.O.; Beese, A.M.; Wilson-Heid, A.; De, A.; Zhang, W. Additive manufacturing of metallic components—Process, structure and properties. *Prog. Mater. Sci.* **2018**, *92*, 112–224. [CrossRef]
15. Wei, H.L.; Mukherjee, T.; Zhang, W.; Zuback, J.S.; Knapp, G.L.; De, A.; DebRoy, T. Mechanistic models for additive manufacturing of metallic components. *Prog. Mater. Sci.* **2021**, *116*, 100703. [CrossRef]
16. Milewski, J.O. *Additive Manufacturing of Metals: From Fundamental Technology to Rocket Nozzles, Medical Implants, and Custom Jewelry*; Springer: London, UK, 2017.
17. Bevans, B.; Barrett, C.; Spears, T.; Gaikwad, A.; Riensche, A.; Smoqi, Z.; Halliday, H.; Rao, P.H.L.D. Heterogeneous sensor data fusion for multiscale, shape agnostic flaw detection in laser powder bed fusion additive manufacturing. *Virtual Phys. Prototyp.* **2023**, *18*, 2196266. [CrossRef]
18. Sanaei, N.; Fatemi, A. Defects in additive manufactured metals and their effect on fatigue performance: A state-of-the-art review. *Prog. Mater. Sci.* **2021**, *117*, 100724. [CrossRef]

19. Singla, A.K.; Banerjee, M.; Sharma, A.; Singh, J.; Bansal, A.; Gupta, M.K.; Khanna, N.; Shahi, A.S.; Goyal, D.K. Selective laser melting of Ti6Al4V alloy: Process parameters, defects and post-treatments. *J. Manuf. Process.* **2021**, *64*, 161–187. [CrossRef]
20. Wang, L.; Yu, Y.; Hu, D.; Yan, W. Multiscale modeling applied to additive manufacturing. In *Fundamentals of Multiscale Modeling of Structural Materials*; Elseiver: Amsterdam, The Netherlands, 2023; pp. 333–388.
21. Sun, C.; Wang, Y.; McMurtrey, M.D.; Jerred, N.D.; Liou, F.; Li, J. Additive manufacturing for energy: A review. *Appl. Energy* **2021**, *28*, 2116041. [CrossRef]
22. Sharma, S.; Joshi, S.S.; Pantawane, M.V.; Radhakrishnan, M.; Mazumder, S.; Dahotre, N.B. Multiphysics multi-scale computational framework for linking process–structure–property relationships in metal additive manufacturing: A critical review. *Int. Mater. Rev.* **2023**, *68*, 1–67. [CrossRef]
23. Zaeh, M.F.; Branner, G. Investigations on residual stresses and deformations in selective laser melting. *Prod. Eng.* **2009**, *4*, 35–45. [CrossRef]
24. Papadakis, L.; Branner, G.; Schober, A.; Richter, K.H.; Uihlein, T. Numerical Modeling of Heat Effects during Thermal Manufacturing of Aero Engine Components. In Proceedings of the World Congress on Engineering, London, UK, 4–6 July 2012.
25. Berry, J.; Perron, A.; Fattebert, J.-L.; Roehling, J.D.; Vrancken, B.; Roehling, T.T.; Rosas, D.L.; Turner, J.A.; Khairallah, S.A.; McKeown, J.T.; et al. Toward multiscale simulations of tailored microstructure formation in metal additive manufacturing. *Mater. Today* **2021**, *51*, 65–86. [CrossRef]
26. Papadakis, L. Modeling and simulation of additive manufacturing processes with metallic powders—Potentials and limitations demonstrated on application examples. In *Additive Manufacturing*; Elseiver: Amsterdam, The Netherlands, 2021; pp. 685–721.
27. Markl, M.; Körner, C. Multiscale Modeling of Powder Bed–Based Additive Manufacturing. *Annu. Rev. Mater. Res.* **2016**, *46*, 93–123. [CrossRef]
28. Promoppatum, P.; Uthaisangsuk, V. Part scale estimation of residual stress development in laser powder bed fusion additive manufacturing of Inconel 718. *Finite Elem. Anal. Des.* **2021**, *189*, 103528. [CrossRef]
29. Francois, M.M.; Sun, A.; King, W.E.; Henson, N.; Tourret, D.; Bronkhorst, C.; Carlson, N.N.; Newman, C.; Haut, T.; Bakosi, J.; et al. Modeling of Additive Manufacturing Processes for Metals: Challenges and Opportunities. *Curr. Opin. Solid State Mater. Sci.* **2017**, *21*, 198–206. [CrossRef]
30. Ahmed, N.; Barsoum, I.; Haidemenopoulos, G.; Al-Rub, R.K.A. Process parameter selection and optimization of laser powder bed fusion for 316L stainless steel: A review. *J. Manuf. Process.* **2022**, *75*, 415–434. [CrossRef]
31. Yang, Y.; Knol, M.F.; van Keulen, F.; Ayas, C. A semi-analytical thermal modelling approach for selective laser melting. *Addit. Manuf.* **2018**, *21*, 284–297. [CrossRef]
32. Yang, Y.; Ayas, C. Point, surface and volumetric heat sources in the thermal modelling of selective laser melting. *Conf. Proc.* **2017**, *1896*, 040006.
33. Darmadi, D.B.; Norrish, J.; Tieu, A.K. Analytic and Finite Element Solutions for Temperature Profiles in Welding using Varied Heat Source Models. *Int. Rev. Mech. Eng.* **2011**, *11*, 8.
34. Rosenthal, D. The Theory of Moving Sources of Heat and Its Application to Metal Treatments. *Trans. Am. Soc. Mech. Eng.* **1946**, *68*, 849–865. [CrossRef]
35. Goldak, J.A.; Akhlaghi, M. *Computational Welding Mechanics*; Springer: London, UK, 2005.
36. Huang, Y. Comprehensive Analytical Modeling of Laser Powder Bed Fed Additive Manufacuting Processes. Ph.D. Thesis, University of Waterloo, Waterloo, ON, Canada, 2019.
37. Yang, J.; Han, J.; Yu, H.; Yin, J.; Gao, M.; Wang, Z.; Zeng, X. Role of molten pool mode on formability, microstructure and mechanical properties of selective laser melted Ti-6Al-4V alloy. *Mater. Des.* **2016**, *110*, 558–570. [CrossRef]
38. Megahed, M.; Mindt, H.-W.; Willems, J.; Dionne, P.; Jacquemetton, L.; Craig, J.; Ranade, P.; Peralta, A. LPBF Right the First Time—The Right Mix Between Modeling and Experiments. *Integr. Mater. Manuf. Innov.* **2019**, *8*, 194–216. [CrossRef]
39. King, W.E.; Anderson, A.T.; Ferencz, R.M.; Hodge, N.E.; Kamath, C.; Khairallah, S.A.; Rubenchik, A.M. Laser powder bed fusion additive manufacturing of metals; physics, computational, and materials challenges. *Appl. Phys. Rev.* **2015**, *2*, 041304. [CrossRef]
40. Cook, P.S.; Murphy, A.B. Simulation of melt pool behaviour during additive manufacturing: Underlying physics and progress. *Addit. Manuf.* **2020**, *31*, 100909. [CrossRef]
41. Zhang, Y.; Chen, Q.; Guillemot, G.; Gandin, C.-A.; Bellet, M. Numerical modelling of fluid and solid thermomechanics in additive manufacturing by powder-bed fusion: Continuum and level set formulation applied to track- and part-scale simulations. *Comptes Rendus Mécanique* **2018**, *346*, 1055–1071. [CrossRef]
42. Fabbro, R. Physical mechanisms controlling keyhole and melt pool dynamics during laser welding. In *Advances in Laser Materials Processing*; Elseiver: Amsterdam, The Netherlands, 2010; pp. 211–241.
43. Qi, T.; Zhu, H.; Zhang, H.; Yin, J.; Ke, L.; Zeng, X. Selective laser melting of Al7050 powder: Melting mode transition and comparison of the characteristics between the keyhole and conduction mode. *Mater. Des.* **2017**, *135*, 257–266. [CrossRef]
44. Lei, Z.; Bi, J.; Chen, Y.; Chen, X.; Qin, X.; Tian, Z. Effect of energy density on formability, microstructure and micro-hardness of selective laser melted Sc- and Zr- modified 7075 aluminum alloy. *Powder Technol.* **2019**, *356*, 594–606. [CrossRef]

45. Gaikwad, A.; Giera, B.; Guss, G.M.; Forien, J.-B.; Matthews, M.J.; Rao, P. Heterogeneous sensing and scientific machine learning for quality assurance in laser powder bed fusion—A single-track study. *Addit. Manuf.* **2020**, *36*, 101659. [CrossRef]
46. King, W.E.; Barth, H.D.; Castillo, V.M.; Gallegos, G.F.; Gibbs, J.W.; Hahn, D.E.; Kamath, C.; Rubenchik, A.M. Observation of keyhole-mode laser melting in laser powder-bed fusion additive manufacturing. *J. Mater. Process. Technol.* **2014**, *214*, 2915–2925. [CrossRef]
47. Semak, V.; Matsunawa, A. The role of recoil pressure in energy balance during laser materials processing. *J. Phys. D Appl. Phys.* **1997**, *30*, 18. [CrossRef]
48. Wu, Y.-C.; San, C.-H.; Chang, C.-H.; Lin, H.-J.; Marwan, R.; Baba, S.; Hwang, W.-S. Numerical modeling of melt-pool behavior in selective laser melting with random powder distribution and experimental validation. *J. Mater. Process. Technol.* **2018**, *254*, 72–78. [CrossRef]
49. Leung, C.L.A.; Marussi, S.; Atwood, R.C.; Towrie, M.; Withers, P.J.; Lee, P.D. In situ X-ray imaging of defect and molten pool dynamics in laser additive manufacturing. *Nat. Commun.* **2018**, *9*, 1355. [CrossRef] [PubMed]
50. Maamoun, A.H.; Xue, Y.F.; Elbestawi, M.A.; Veldhuis, S.C. Effect of Selective Laser Melting Process Parameters on the Quality of Al Alloy Parts: Powder Characterization, Density, Surface Roughness, and Dimensional Accuracy. *Materials* **2018**, *11*, 2343. [CrossRef]
51. Maamoun, A.H.; Xue, Y.F.; Elbestawi, M.A.; Veldhuis, S.C. The Effect of Selective Laser Melting Process Parameters on the Microstructure and Mechanical Properties of Al6061 and AlSi10Mg Alloys. *Materials* **2018**, *12*, 10012. [CrossRef] [PubMed]
52. Radaj, D. *Heat Effects of Welding: Temperature Field, Residual Stress, Distortion*; Springer: London, UK, 1992.
53. Williams, R.J.; Piglione, A.; Rønneberg, T.; Jones, C.; Pham, M.-S.; Davies, C.M.; Hooper, P.A. In situ thermography for laser powder bed fusion: Effects of layer temperature on porosity, microstructure and mechanical properties. *Addit. Manuf.* **2019**, *30*, 100880. [CrossRef]
54. Hooper, P.A. Melt pool temperature and cooling rates in laser powder bed fusion. *Addit. Manuf.* **2018**, *22*, 548–559. [CrossRef]
55. Arısoy, Y.M.; Criales, L.E.; Özel, T. Modeling and simulation of thermal field and solidification in laser powder bed fusion of nickel alloy IN625. *Opt. Laser Technol.* **2019**, *109*, 278–292. [CrossRef]
56. Bayat, M.; Dong, W.; Thorborg, J.; To, A.C.; Hattel, J.H. A review of multi-scale and multi-physics simulations of metal additive manufacturing processes with focus on modeling strategies. *Addit. Manuf.* **2021**, *47*, 102278. [CrossRef]
57. Parry, L.; Ashcroft, I.A.; Wildman, R.D. Understanding the effect of laser scan strategy on residual stress in selective laser melting through thermo-mechanical simulation. *Addit. Manuf.* **2016**, *12*, 1–15. [CrossRef]
58. Martukanitz, R.; Michaleris, P.; Palmer, T.; DebRoy, T.; Liu, Z.-K.; Otis, R.; Heo, T.W.; Chen, L.-Q. Toward an integrated computational system for describing the additive manufacturing process for metallic materials. *Addit. Manuf.* **2014**, *1–4*, 52–63. [CrossRef]
59. Yan, W.; Lian, Y.; Yu, C.; Kafka, O.L.; Liu, Z.; Liu, W.K.; Wagner, G.J. An integrated process–structure–property modeling framework for additive manufacturing. *Comput. Methods Appl. Mech. Eng.* **2018**, *339*, 184–204. [CrossRef]
60. Zhang, Y.; Zhang, J. Modeling of solidification microstructure evolution in laser powder bed fusion fabricated 316L stainless steel using combined computational fluid dynamics and cellular automata. *Addit. Manuf.* **2019**, *28*, 750–765. [CrossRef]
61. Lian, Y.; Gan, Z.; Yu, C.; Kats, D.; Liu, W.K.; Wagner, G.J. A cellular automaton finite volume method for microstructure evolution during additive manufacturing. *Mater. Des.* **2019**, *169*, 107672. [CrossRef]
62. Elangeswaran, C.; Cutolo, A.; Gallas, S.; Dinh, T.D.; Lammens, N.; Erdelyi, H.; Schulz, M.; Muralidharan, G.K.; Thijs, L.; Craeghs, T.; et al. Predicting fatigue life of metal LPBF components by combining a large fatigue database for different sample conditions with novel simulation strategies. *Addit. Manuf.* **2022**, *50*, 102570. [CrossRef]
63. Oliveira, J.P.; Santos, T.G.; Miranda, R.M. Revisiting fundamental welding concepts to improve additive manufacturing: From theory to practice. *Prog. Mater. Sci.* **2020**, *107*, 100590. [CrossRef]
64. Riensche, A.R.; Bevans, B.D.; King, G.; Krishnan, A.; Cole, K.D.; Rao, P. Predicting meltpool depth and primary dendritic arm spacing in laser powder bed fusion additive manufacturing using physics-based machine learning. *Mater. Des.* **2024**, *237*, 112540. [CrossRef]
65. Promoppatum, P.; Yao, S.-C.; Pistorius, P.C.; Rollett, A.D. A Comprehensive Comparison of the Analytical and Numerical Prediction of the Thermal History and Solidification Microstructure of Inconel 718 Products Made by Laser Powder-Bed Fusion. *Engineering* **2017**, *3*, 685–694. [CrossRef]
66. Cole, K.D.; Riensche, A.; Rao, P.K. Discrete Green's functions and spectral graph theory for computationally efficient thermal modeling. *Int. J. Heat Mass Transf.* **2022**, *183*, 122112. [CrossRef]
67. Bayat, M.; Klingaa, C.G.; Mohanty, S.; De Baere, D.; Thorborg, J.; Tiedje, N.S.; Hattel, J.H. Part-scale thermo-mechanical modelling of distortions in Laser Powder Bed Fusion—Analysis of the sequential flash heating method with experimental validation. *Addit. Manuf.* **2020**, *36*, 101508. [CrossRef]
68. Moran, T.P.; Warner, D.H.; Phan, N. Scan-by-scan part-scale thermal modelling for defect prediction in metal additive manufacturing. *Addit. Manuf.* **2021**, *37*, 101667. [CrossRef]

69. Moran, T.P.; Li, P.; Warner, D.H.; Phan, N. Utility of superposition-based finite element approach for part-scale thermal simulation in additive manufacturing. *Addit. Manuf.* **2018**, *21*, 215–219. [CrossRef]
70. Holman, J. *Heat Transfer*, 10th ed.; McGraw Hill: New York City, NY, USA, 2010.
71. Gouge, M.; Denlinger, E.; Irwin, J.; Li, C.; Michaleris, P. Experimental validation of thermo-mechanical part-scale modeling for laser powder bed fusion processes. *Addit. Manuf.* **2019**, *29*, 100771. [CrossRef]
72. Zhang, W.; Tong, M.; Harrison, N.M. Resolution, energy and time dependency on layer scaling in finite element modelling of laser beam powder bed fusion additive manufacturing. *Addit. Manuf.* **2019**, *28*, 610–620. [CrossRef]
73. Williams, R.J.; Davies, C.M.; Hooper, P.A. A pragmatic part scale model for residual stress and distortion prediction in powder bed fusion. *Addit. Manuf.* **2018**, *22*, 416–425. [CrossRef]
74. Ganeriwala, R.K.; Strantza, M.; King, W.E.; Clausen, B.; Phan, T.Q.; Levine, L.E.; Brown, D.W.; Hodge, N.E. Evaluation of a thermomechanical model for prediction of residual stress during laser powder bed fusion of Ti-6Al-4V. *Addit. Manuf.* **2019**, *27*, 489–502. [CrossRef]
75. Hodge, N.E.; Ferencz, R.M.; Vignes, R.M. Experimental comparison of residual stresses for a thermomechanical model for the simulation of selective laser melting. *Addit. Manuf.* **2016**, *12*, 159–168. [CrossRef]
76. Liang, X.; Cheng, L.; Chen, Q.; Yang, Q.; To, A.C. A modified method for estimating inherent strains from detailed process simulation for fast residual distortion prediction of single-walled structures fabricated by directed energy deposition. *Addit. Manuf.* **2018**, *23*, 471–486. [CrossRef]
77. Xie, D.; Lv, F.; Yang, Y.; Shen, L.; Tian, Z.; Shuai, C.; Chen, B.; Zhao, J. A Review on Distortion and Residual Stress in Additive Manufacturing. *Chin. J. Mech. Eng. Addit. Manuf. Front.* **2022**, *1*, 100039. [CrossRef]
78. Liang, X.; Chen, Q.; Cheng, L.; Hayduke, D.; To, A.C. Modified inherent strain method for efficient prediction of residual deformation in direct metal laser sintered components. *Comput. Mech.* **2019**, *64*, 1719–1733. [CrossRef]
79. Ueda, Y.; Fukuda, K.; Tanigawa, M. New Measuring Method of Three Dimensional Residual Stresses Based on Theory of Inherent Strain. *Trans. JWRI* **1979**, *8*, 249–256.
80. Ueda, Y.; Fukuda, K.; Kim, Y.C. New Measuring Method of Axisymmetric Three-Dimensional Residual Stresses Using Inherent Strains as Parameters. *J. Eng. Mater. Technol.* **1986**, *108*, 328–334. [CrossRef]
81. Chen, Q.; Liang, X.; Hayduke, D.; Liu, J.; Cheng, L.; Oskin, J.; Whitmore, R.; To, A.C. An inherent strain based multiscale modeling framework for simulating part-scale residual deformation for direct metal laser sintering. *Addit. Manuf.* **2019**, *28*, 406–418. [CrossRef]
82. Dong, W.; Liang, X.; Chen, Q.; Hinnebusch, S.; Zhou, Z.; To, A.C. A new procedure for implementing the modified inherent strain method with improved accuracy in predicting both residual stress and deformation for laser powder bed fusion. *Addit. Manuf.* **2021**, *47*, 102345. [CrossRef]
83. Michaleris, P. Modeling metal deposition in heat transfer analyses of additive manufacturing processes. *Finite Elem. Anal. Des.* **2014**, *86*, 51–60. [CrossRef]
84. Dong, W.; Jimenez, X.A.; To, A.C. Temperature-dependent modified inherent strain method for predicting residual stress and distortion of Ti6Al4V walls manufactured by wire-arc directed energy deposition. *Addit. Manuf.* **2023**, *62*, 103386. [CrossRef]
85. Bellet, M.; Tematio, J.K.; Zhang, Y. The inherent strain method for additive manufacturing: Critical analysis and new inherent strain rate method. *IOP Conf. Ser. Mater. Sci. Eng.* **2023**, *1281*, 012001. [CrossRef]
86. Bellet, M.; Keumo Tematio, J.; Zhang, Y. The inherent strain rate method for thermo-mechanical simulation of directed energy deposition additive manufacturing. *Int. J. Numer. Methods Eng.* **2023**, *124*, 4058–4074. [CrossRef]
87. Doghri, I. *Mechanics of Deformable Solids: Linear, Nonlinear, Analytical and Computational Aspects*; Springer: London, UK, 2000.
88. Badiru, A.B.; Valencia, V.V.; Liu, D. *Additive Manufacturing Handbook Product Development for the Defense Industry*; Badiru, A.B., Valencia, V.V., Liu, D., Eds.; CRC Press: Boca Raton, FL, USA, 2017.
89. Lian, Y.; Lin, S.; Yan, W.; Liu, W.K.; Wagner, G.J. A parallelized three-dimensional cellular automaton model for grain growth during additive manufacturing. *Comput. Mech.* **2018**, *61*, 543–558. [CrossRef]
90. Zinoviev, A.; Zinovieva, O.; Ploshikhin, V.; Romanova, V.; Balokhonov, R. Evolution of grain structure during laser additive manufacturing. Simulation by a cellular automata method. *Mater. Des.* **2016**, *106*, 321–329. [CrossRef]
91. Guo, Z.; Zhou, J.; Yin, Y.; Shen, X.; Ji, X. Numerical Simulation of Three-Dimensional Mesoscopic Grain Evolution: Model Development, Validation, and Application to Nickel-Based Superalloys. *Metals* **2019**, *9*, 10057. [CrossRef]
92. Bresson, Y.; Tongne, A.; Baili, M.; Arnaud, L. Global-to-local simulation of the thermal history in the laser powder bed fusion process based on a multiscale finite element approach. *Int. J. Adv. Manuf. Technol.* **2023**, *127*, 4727–4744. [CrossRef]
93. Pal, D.; Patil, N.; Zeng, K.; Stucker, B. An Integrated Approach to Additive Manufacturing Simulations Using Physics Based, Coupled Multiscale Process Modeling. *J. Manuf. Sci. Eng.* **2014**, *136*, 061022. [CrossRef]
94. O'Toole, P.I.; Patel, M.J.; Tang, C.; Gunasegaram, D.; Murphy, A.B.; Cole, I.S. Multiscale simulation of rapid solidifi cation of an aluminium–silicon alloy under additive manufacturing conditions. *Addit. Manuf.* **2021**, *48*, 102353. [CrossRef]

95. Mollamahmutoglu, M.; Yilmaz, O.; Unal, R.; Gumus, B.; Tan, E. The effect of evaporation and recoil pressure on energy loss and melt pool profile in selective electron beam melting. *Int. J. Adv. Manuf. Technol.* **2022**, *120*, 4041–4050. [CrossRef]
96. Ninpetch, P.; Kowitwarangkul, P.; Chalermkarnnon, P.; Promoppatum, P.; Chuchuay, P.; Rattanadecho, P. Numerical Modeling of Distortion of Ti-6Al-4V Components Manufactured Using Laser Powder Bed Fusion. *Metals* **2022**, *12*, 91484. [CrossRef]
97. Mukherjee, T.; Wei, H.L.; De, A.; DebRoy, T. Heat and fluid flow in additive manufacturing—Part I: Modeling of powder bed fusion. *Comput. Mater. Sci.* **2018**, *150*, 304–313. [CrossRef]
98. Liu, J.; Wen, P. Metal vaporization and its influence during laser powder bed fusion process. *Mater. Des.* **2022**, *215*, 110505. [CrossRef]
99. Klassen, A.; Scharowsky, T.; Körner, C. Evaporation model for beam based additive manufacturing using free surface lattice Boltzmann methods. *J. Phys. D Appl. Phys.* **2014**, *47*, 275303. [CrossRef]
100. Fish, J.; Belytschko, T. *A First Course in Finite Elements*; Wiley: Hoboken, NJ, USA, 2007.
101. Schoinochoritis, B.; Chantzis, D.; Salonitis, K. Simulation of metallic powder bed additive manufacturing processes with the finite element method: A critical review. *Proc. Inst. Mech. Eng. Part B J. Eng. Manuf.* **2016**, *231*, 96–117. [CrossRef]
102. Yang, Q.C.; Zhang, P.; Cheng, L.; Min, Z.; Chyu, M.; To, A.C. Finite element modeling and validation of thermomechanical behavior of Ti-6Al-4V in directed energy deposition additive manufacturing. *Addit. Manuf.* **2016**, *12*, 169–177. [CrossRef]
103. Mayer, T.; Brandle, G.; Schonenberger, A.; Eberlein, R. Simulation and validation of residual deformations in additive manufacturing of metal parts. *Heliyon* **2020**, *6*, e03987. [CrossRef]
104. ANSYS. *Additive Calibration Guide*; ANSYS: Canonsburg, PA, USA, 2021.
105. ANSYS. *ANSYS Workbench Additive Manufacturing Analysis Guide*; ANSYS: Canonsburg, PA, USA, 2021.
106. Weber, S.; Montero, J.; Bleckmann, M.; Paetzold, K. A Comparison of Layered Tetrahedral and Cartesian meshing in Additive Manufacturing Simulation. *Procedia CIRP* **2020**, *91*, 522–527. [CrossRef]
107. Moges, T.; Ameta, G.; Witherell, P. A Review of Model Inaccuracy and Parameter Uncertainty in Laser Powder Bed Fusion Models and Simulations. *J. Manuf. Sci. Eng.* **2019**, *141*, 040801. [CrossRef] [PubMed]
108. Vanini, M.; Searle, S.; Vanmeensel, K.; Vrancken, B. Avoiding heat source calibration for finite element modeling of the laser powder bed fusion process. *Addit. Manuf.* **2024**, *92*, 104369. [CrossRef]
109. DebRoy, T.; David, S.A. Physical processes in fusion welding. *Rev. Mod. Phys.* **1995**, *67*, 85–112. [CrossRef]
110. Manvatkar, V.; De, A.; DebRoy, T. Heat transfer and material flow during laser assisted multi-layer additive manufacturing. *J. Appl. Phys.* **2014**, *116*, 124905. [CrossRef]
111. Chen, F.; Yan, W. High-fidelity modelling of thermal stress for additive manufacturing by linking thermal-fluid and mechanical models. *Mater. Des.* **2020**, *196*, 109185. [CrossRef]
112. FlowScience. *FLOW-3D User Manual, Release 2022R2*; FlowScience: Santa Fe, NM, USA, 2022.
113. Lee, Y.S.; Zhang, W. Modeling of heat transfer, fluid flow and solidification microstructure of nickel-base superalloy fabricated by laser powder bed fusion. *Addit. Manuf.* **2016**, *12*, 178–188. [CrossRef]
114. Yan, W.; Ge, W.; Qian, Y.; Lin, S.; Zhou, B.; Liu, W.K.; Lin, F.; Wagner, G.J. Multi-physics modeling of single/multiple-track defect mechanisms in electron beam selective melting. *Acta Mater.* **2017**, *134*, 324–333. [CrossRef]
115. Bayat, M.; Mohanty, S.; Hattel, J.H. Multiphysics modelling of lack-of-fusion voids formation and evolution in IN718 made by multi-track/multi-layer L-PBF. *Int. J. Heat Mass Transf.* **2019**, *139*, 95–114. [CrossRef]
116. Bayat, M.; Thanki, A.; Mohanty, S.; Witvrouw, A.; Yang, S.; Thorborg, J.; Tiedje, N.S.; Hattel, J.H. Keyhole-induced porosities in Laser-based Powder Bed Fusion (L-PBF) of Ti6Al4V: High-fidelity modelling and experimental validation. *Addit. Manuf.* **2019**, *30*, 100835. [CrossRef]
117. Li, E.; Zhou, Z.; Wang, L.; Zou, R.; Yu, A. Modelling of keyhole dynamics and melt pool flow in laser powder bed fusion process. *Powder Technol.* **2022**, *400*, 117262. [CrossRef]
118. Hirt, C.; Nichols, B. Volume of Fluid (VOF) Method for the Dynamics of Free Boundaries. *J. Comput. Phys.* **1981**, *39*, 201–225. [CrossRef]
119. Katopodes, N.D. Volume of Fluid Method. In *Free-Surface Flow*; Elseiver: Amsterdam, The Netherlands, 2019; pp. 766–802.
120. Mohd Yusuf, S.; Cutler, S.; Gao, N. Review: The Impact of Metal Additive Manufacturing on the Aerospace Industry. *Metals* **2019**, *9*, 1286. [CrossRef]
121. Chang, K.-H. *E-Design: Computer-Aided Engineering Design*, 1st ed.; Elsvier: Amsterdam, The Netherlands, 2016.
122. Dordlofva, C. A Design for Qualification Framework for the Development of Additive Manufacturing Components—A Case Study from the Space Industry. *Aerospace* **2020**, *7*, 30025. [CrossRef]
123. Taylor, H.C.; Garibay, E.A.; Wicker, R.B. Toward a common laser powder bed fusion qualification test artifact. *Addit. Manuf.* **2021**, *39*, 101803. [CrossRef]
124. Seifi, M.; Gorelik, M.; Waller, J.; Hrabe, N.; Shamsaei, N.; Daniewicz, S.; Lewandowski, J.J. Progress Towards Metal Additive Manufacturing Standardization to Support Qualification and Certification. *J. Miner. Met. Mater. Soc.* **2017**, *69*, 439–455. [CrossRef]

125. *ISO/ASTM 52900:2021*; Additive Manufacturing—General Principles—Fundamentals and Vocabulary. ISO/ASTM International: Geneva, Switzerland, 2021.
126. *ISO/ASTM 52901:2017*; Additive Manufacturing—General Principles—Requirements for Purchased AM Parts. ISO/ASTM International: Geneva, Switzerland, 2017.
127. *ISO/ASTM 52902:2023*; Additive Manufacturing—Test Artefacts—Geometric Capability Assessment of Additive Manufacturing Systems. ISO/ASTM International: Geneva, Switzerland, 2023.
128. *ISO/ASTM 52904:2024*; Additive Manufacturing of Metals—Process Characteristics and Performance—Metal Powder Bed Fusion Process to Meet Critical Applications. ISO/ASTM International: Geneva, Switzerland, 2024.
129. *ISO/ASTM TR 52905:2023*; Additive Manufacturing of Metals—Non-Destructive Testing and Evaluation—Defect Detection in Parts. ISO/ASTM International: Geneva, Switzerland, 2023.
130. *ISO/ASTM 52908:2023*; Additive Manufacturing of Metals—Finished Part Properties—Post-Processing, Inspection and Testing of Parts Produced by Powder Bed Fusion. ISO/ASTM International: Geneva, Switzerland, 2023.
131. *ISO/ASTM 52920:2023*; Additive Manufacturing—Qualification Principles—Requirements for Industrial Additive Manufacturing Processes and Production Sites. ISO/ASTM International: Geneva, Switzerland, 2023.
132. *ISO/ASTM TS 52930:2021*; Additive Manufacturing—Qualification Principles—Installation, Operation and Performance (IQ/OQ/PQ) of PBF-LB Equipment. ISO/ASTM International: Geneva, Switzerland, 2021.
133. *ISO/ASTM 52941:2020*; Additive Manufacturing—System Performance and Reliability—Acceptance Tests for Laser Metal Powder-Bed Fusion Machines for Metallic Materials for Aerospace Application. ISO/ASTM International: Geneva, Switzerland, 2020.
134. *ISO/ASTM 52942:2020*; Additive Manufacturing—Qualification Principles—Qualifying Machine Operators of Laser Metal Powder Bed Fusion Machines And Equipment Used in Aerospace Applications. ISO/ASTM International: Geneva, Switzerland, 2020.
135. *ISO/ASTM 52950:2021*; Additive Manufacturing—General Principles—Overview of Data Processing. ISO/ASTM International: Geneva, Switzerland, 2021.
136. *ASTM F3530-22*; Standard Guide for Additive Manufacturing—Design Strategies for Part Consolidation. ASTM International: West Conshohocken, PA, USA, 2022.
137. *ASTM F3572-22*; Standard Practice for Additive Manufacturing—General Principles—Part Classifications for Additive Manufactured Parts Used in Aviation. ASTM International: West Conshohocken, PA, USA, 2022.
138. *ASTM F3592-23*; Standard Practice for Additive Manufacturing—Qualification of AM Systems. ASTM International: West Conshohocken, PA, USA, 2023.
139. *ASTM F3626-23*; Standard Test Method for Additive Manufacturing—Nondestructive Evaluation of AM Parts. ASTM International: West Conshohocken, PA, USA, 2023.
140. *SAE AMS7003A*; Additive Manufacturing—Laser Powder Bed Fusion Process. SAE International: Warrendale, PA, USA, 2022.
141. *SAE AMS7032*; Machine Qualification for Fusion-Based Metal Additive Manufacturing Processes. SAE International: Warrendale, PA, USA, 2023.
142. *SAE AMS7002A*; Additive Manufacturing—General Requirements for Additive Manufacturing of Metal Parts. SAE International: Warrendale, PA, USA, 2023.
143. *AWS D20.1/D20.1M:2019*; Specification for Fabrication of Metal Components Using Additive Manufacturing. American Welding Society: Miami, FL, USA, 2019.
144. *SAE AIR7352*; Additive Manufacturing—Design Guidelines for Aerospace Components. SAE International: Warrendale, PA, USA, 2023.
145. *DIN 65123:2023*; Additive Manufacturing—Process Requirements and Quality Assurance for Powder Bed Fusion of Metallic Materials. Deutsches Institut für Normung: Berlin, Germany, 2023.
146. *DIN 65124:2023*; Additive Manufacturing—Guidelines for Post-Processing and Quality Assurance of Additively Manufactured Parts. Deutsches Institut für Normung: Berlin, Germany, 2023.